Blended isogeometric Kirchhoff–Love and continuum shells

Ning Liu[a,*], Emily L. Johnson[b], Manoj R. Rajanna[b], Jim Lua[a], Nam Phan[c], Ming-Chen Hsu[b]

[a]*Global Engineering & Materials, Inc., Princeton, New Jersey 08540, USA*
[b]*Department of Mechanical Engineering, Iowa State University, Ames, Iowa 50011, USA*
[c]*Structures Division, Naval Air Systems Command (NAVAIR), Patuxent River, Maryland 20670, USA*

Abstract

The computational modeling of thin-walled structures based on isogeometric analysis (IGA), non-uniform rational B-splines (NURBS), and Kirchhoff–Love (KL) shell formulations has attracted significant research attention in recent years. While these methods offer numerous benefits over the traditional finite element approach, including exact representation of the geometry, naturally satisfied high-order continuity within each NURBS patch, and computationally efficient rotation-free formulations, they also present a number of challenges in modeling real-world engineering structures of considerable complexity. Specifically, these NURBS-based engineering models are usually comprised of numerous patches, with discontinuous derivatives, non-conforming discretizations, and non-watertight connections at their interfaces. Moreover, the analysis of such structures often requires the full stress and strain tensors (i.e., including the transverse normal and shear components) for subsequent failure analysis and remaining life prediction. Despite the efficiency provided by the KL shell, the formulation cannot accurately predict the response in the transverse directions due to its kinematic assumptions. In this work, a penalty-based formulation for the blended coupling of KL and continuum shells is presented. The proposed approach embraces both the computational efficiency of KL shells and the availability of the full-scale stress/strain tensors of continuum shells where needed by modeling critical structural components using continuum shells and other components using KL shells. The proposed method enforces the displacement and rotational continuities in a variational manner and is applicable to non-conforming and non-smooth interfaces. The efficacy of the developed method is demonstrated through a number of benchmark studies with a variety of analysis configurations, including linear and nonlinear analyses, matching and non-matching discretizations, and isotropic and composite materials. Finally, an aircraft horizontal stabilizer is considered to demonstrate the applicability of the proposed blended shells to real-world engineering structures of significant complexity.

Keywords: isogeometric analysis; Kirchhoff–Love shell; continuum shell; patch coupling; penalty method; non-matching discretization

---

*Corresponding author
Email addresses:* `nliu@gem-innovation.com` (Ning Liu), `jmchsu@iastate.edu` (Ming-Chen Hsu)

Contents

1. Introduction

Isogeometric analysis (IGA), introduced by Hughes et al. [1], was originally proposed to bridge the gap between computer-aided geometric design (CAGD) models, which are often constructed using non-uniform rational B-splines (NURBS) [2] and recently using other spline technologies [3–16], and their corresponding physics-based computational approximation models that are frequently based on Lagrange polynomial representations for the geometry and solution spaces. The essential concept of IGA is to employ the same basis functions that are used in design for numerical analysis. The IGA approach has since been used to solve the most challenging science and engineering problems [17–28], and it has been demonstrated in a variety of applications that the high-order smoothness of spline basis functions in IGA is superior to the C^0-continuity of the shape functions in traditional finite element analysis [29–38]. This is also true in the realm of Kirchhoff–Love (KL) shell analysis, where IGA has emerged as an ideal platform in the sense that the global C^1-continuity requirement resulting from the second-order differential operators in the primal variational form can be naturally satisfied through the use of higher-order spline basis functions. Thus, isogeometric KL shells [39–47] have gained popularity in the simulation and analysis community due to their computationally efficient rotation-free formulation and model simplification into the midsurface representation. The formulations have been previously demonstrated as an effective

solution for the analysis of complex problems [48–61], including wind turbine blades [62–72] and heart valves [73–81]. While computational efficiency is an important factor in numerical analysis, KL shells have limited accuracy in predicting the transverse stress and strain states. This limitation has sparked the development of IGA-based continuum shell and layerwise continuous shell formulations [82–89], which enable other analysis types where stress triaxiality effects cannot be neglected, such as multiaxial fatigue analysis [90] and ductile fracture analysis [91].

Real-world CAGD models are usually comprised of multiple patches. Such multi-patch descriptions are typically required when the engineering model includes topological characteristics or geometric discontinuities that cannot be captured with a single spline patch. Distinct patches in a single model can also be used to distinguish various design features, such as a change in functionality or representation of material dissimilarity. As a result, the aforementioned shell formulations cannot be readily applied for analysis without special treatment at the interface between two joined patches. Specifically, interfacial displacement and rotational continuities are often required. This can be easily achieved in the case of matching patch discretizations, where one can simply merge or tie the control points at the common boundary to enforce displacement continuity and apply explicit geometric constraints to the first two rows of control points to retain derivative continuity [39, 92]. However, this type of manually applied constraint manipulation is cumbersome and is not applicable to more general cases where the interface may be non-conforming. Ideally, an approach that is able to impose both displacement and rotational continuities irrespective of the interface smoothness and discretization conditions is highly desired.

Driven by the need to perform shell analysis directly on multi-patch NURBS objects, a significant amount of effort has been devoted to developing new techniques for patch coupling. Among others, constraining the relative motions in terms of displacements and rotations at the common boundary in the spirit of penalty methods has become a common approach to couple patches. For instance, the bending strip method was proposed to connect patches by adding fictitious strips of unidirectional bending stiffness [93, 94]. However, this approach is restricted to matching discretizations. The work of Lei et al. [95] coupled surfaces by virtually inserting control points to make the interface matching and subsequently applying linear constraints to the virtually matched interface, and similar approaches have been reported [96]; however, these methods are limited in terms of patch configurations and cannot be applied to non-smooth patch interfaces. Instead of enforcing rotational continuity through explicit geometric constraints, a more general penalty formulation based on including the penalty contribution in the principle of virtual work was proposed [48] and later extended to Reissner–Mindlin shells [97]. Nevertheless, this method restricted the rotation at the patch boundary to be less than 90° and has limited applicability in large displacement analysis. Duong et al. [98] presented a penalty formulation to preserve the angle at the patch interface, but it is restricted to matching discretization with problem-specific penalty param-

eters. More recently, Herrema et al. [99] proposed a penalty coupling formulation in a variational framework. The method does not require the penalty parameter to be manually selected and is suitable for non-matching and non-smooth interfaces. The applicability of the method has been demonstrated in the modeling of complex, real-world composite wind turbine blades [38, 72] and transcatheter heart valves [100]. The convergence of the method was further improved in Leonetti et al. [101] by rewriting the penalty energies in a Hellinger–Reissner sense to introduce conjugate field work to the coupled system.

In addition to the penalty approaches, there are also a variety of other methods that can be utilized for patch coupling. For instance, Nitsche's method has been investigated for the coupling of non-matching and trimmed patches [102] and has been successfully extended to pure KL shell and blended shell couplings [103, 104], as well as in the nonlinear analysis setting [54, 105]. While this method is quite promising, the derivation of the formulation depends on the specific variational form of the problem. Additionally, so-called Mortar methods have also been studied to couple IGA patches [106–108]. However, the determination of the Lagrange multiplier spaces in this method requires solving a computationally challenging saddle point problem. This approach has been recently extended in the form of a basis modification approach based on a least-square formulation to avoid the complicated segmentation process [109]. A blended shell formulation that couples KL shells with Reissner–Mindlin shells, in which the rotational degrees of freedom can be selectively added to allow patches to be connected, has also been proposed [31].

The present work builds upon the previous KL shell coupling approach and develops a penalty-based formulation for coupling non-matching patches at a blended coupling interface between isogeometric KL and continuum shells. The goal of this formulation is to achieve high-fidelity, three-dimensional (3D) stress/strain prediction at critical structural components using continuum shells while modeling the rest of the structures using KL shells to retain computational efficiency. Compared to previous methods, the proposed penalty formulation represents a unified patch coupling approach that can be easily applied to many different shell models. The proposed formulation is used to impose both displacement and rotational continuities in the multi-patch blended shell analysis. Analogous to the previous penalty-based patch coupling method for KL shells, the efficacy of the present method is controlled by a single dimensionless penalty parameter. To eliminate the empirical determination of the problem-specific penalty parameters based on a trial-and-error process, the present method considers dimensionally consistent scaling with element size, material properties, and geometric parameters, and thus permits a universal selection of the penalty parameter irrespective of the problem definition. The presented formulation is tested for a variety of problem configurations ranging from matching to non-matching discretizations, linear to nonlinear analyses, and isotropic to composite materials, to demonstrate the accuracy and robustness of the proposed method. Finally, the method is applied to the analysis of an aircraft horizontal stabi-

lizer model, demonstrating the applicability of the proposed blended shell approach to real-world engineering structures of significant complexity.

This paper is outlined as follows. In Section 2, the isogeometric continuum shell, KL shell, and blended coupling formulations are introduced. A detailed discussion on the determination of the single universal penalty parameter is also given. In Section 3, a set of benchmark examples are analyzed to demonstrate the accuracy and robustness of the proposed blended shell coupling formulation. The effectiveness of the universal choice of the penalty parameter is also demonstrated. The proposed method is then applied in Section 4 to the analysis of a horizontal stabilizer model, where a section of the stabilizer skin is modeled using the isogeometric continuum shells and KL shells are deployed elsewhere. Finally, in Section 5, conclusions about the proposed method are drawn.

2. Blended shell formulation

The blended shell method proposed in this work involves the isogeometric continuum shell and composite KL shell formulations. A brief summary of the adopted continuum and KL shell approaches are provided here, with particular details related to the blended coupling aspects. The following notations are used: italic letters (e.g., a, A) indicate scalars, lower case bold letters (e.g., $\mathbf{a}$) indicate vectors, and upper case bold letters (e.g., $\mathbf{A}$) indicate second order tensors. Geometric variables indicated by $\mathring{(\cdot)}$ refer to the undeformed configuration. Compact notation is used only when convenient for the presentation of general equations, while the detailed derivations are written in index notation. The Latin indices i, j, k, and l take on values $\{1, 2, 3\}$, while the Greek indices α and β take on values $\{1, 2\}$; summation convention of repeated indices is used.

2.1. Isogeometric continuum shells

We begin by presenting an isogeometric continuum shell formulation. Let $\mathring{\mathbf{x}}(\xi_1, \xi_2, \xi_3)$ represent the position of a material point within the shell body in the undeformed configuration, where ξ_1 and ξ_2 are the convective curvilinear coordinates in the in-plane directions, and ξ_3 is the through-thickness coordinate. The position vector can be expressed as

$$\mathring{\mathbf{x}}(\xi_1, \xi_2, \xi_3) = \mathring{\mathbf{r}}(\xi_1, \xi_2) + \xi_3 \mathring{\mathbf{a}}_3(\xi_1, \xi_2) \ , \tag{1}$$

where $\mathring{\mathbf{r}}$ is a point on the reference (bottom) surface of the continuum shell, $\xi_3 \in [0, t_h]$ with t_h being the shell thickness, and $\mathring{\mathbf{a}}_3$ is the unit thickness director normal to the shell reference surface. Let $\mathring{\mathbf{a}}_\alpha = \mathring{\mathbf{r}}_{,\alpha}$, where $(\cdot)_{,\alpha} = \partial(\cdot)/\partial \xi_\alpha$, be the base vectors of the reference surface in the undeformed

configuration. $\mathring{\mathbf{a}}_3$ can then be written as

$$\mathring{\mathbf{a}}_3 = \frac{\mathring{\mathbf{a}}_1 \times \mathring{\mathbf{a}}_2}{\left\| \mathring{\mathbf{a}}_1 \times \mathring{\mathbf{a}}_2 \right\|} \ . \tag{2}$$

Remark 1. Without loss of generality, the bottom surface is employed here as the reference surface. While one may pick any surface (e.g., the midsurface) in the continuum shell body as the reference surface, the bottom surface is selected in this work to be consistent with the composite definition. Note also that the proposed blended shell formulation is not dependent on where the reference surface is defined.

The motion of an arbitrary material point in the continuum shell can be more conveniently defined through the introduction of a set of covariant base vectors. The base vectors at any point in the undeformed shell body can be denoted as $\mathring{\mathbf{g}}_i = \mathring{\mathbf{x}}_{,i}$, where $(\cdot)_{,i} = \partial(\cdot)/\partial\xi_i$, and expressed as

$$\mathring{\mathbf{g}}_\alpha = \mathring{\mathbf{a}}_\alpha + \xi_3 \mathring{\mathbf{a}}_{3,\alpha} \ , \tag{3}$$

$$\mathring{\mathbf{g}}_3 = \mathring{\mathbf{a}}_3 \ . \tag{4}$$

Their dual base vectors (i.e., the contravariant basis) can be obtained using $\mathring{\mathbf{g}}_i \cdot \mathring{\mathbf{g}}^j = \delta_i^j$, where δ_i^j is the Kronecker delta. The position of the material point in the deformed configuration, $\mathbf{x}\,(\xi_1, \xi_2, \xi_3)$, is related to $\mathring{\mathbf{x}}$ through the displacement field $\mathbf{u}\,(\xi_1, \xi_2, \xi_3)$ as $\mathbf{x} = \mathring{\mathbf{x}} + \mathbf{u}$. The covariant base vectors in the deformed configuration can be defined as

$$\mathbf{g}_i = \mathbf{x}_{,i} = \mathring{\mathbf{g}}_i + \mathbf{u}_{,i} \ . \tag{5}$$

Finally, the deformation gradient between the undeformed and deformed configurations can be expressed as $\mathbf{F} = \mathbf{g}_i \otimes \mathring{\mathbf{g}}^i$.

In a total Lagrangian framework, the variational formulation of the isogeometric continuum shell can be expressed through the principle of virtual work, where the contribution of the body force is neglected for brevity:

$$\delta W = \delta W^{\text{int}} - \delta W^{\text{ext}} = \int_{\Omega_0} \delta \mathbf{E} : \mathbf{S} \, d\Omega - \int_{\Gamma_0^{\text{h}}} \delta \mathbf{u} \cdot \mathbf{h} \, d\Gamma = 0 \ , \tag{6}$$

where W is the total work, W^{int} is the internal work, W^{ext} is the external work, δ indicates the variation with respect to the virtual displacement variable $\delta\mathbf{u}$, $\mathbf{S}$ is the second Piola–Kirchhoff stress tensor, $\mathbf{E}$ is the Green–Lagrange strain tensor, Ω_0 is the shell volume in the undeformed configuration, $\mathbf{h}$ is the surface traction, and Γ_0^{h} is the undeformed boundary where $\mathbf{h}$ is applied. The

Green–Lagrange strain can be defined as

$$\mathbf{E} = \frac{1}{2}\left(\mathbf{F}^{\mathrm{T}}\mathbf{F} - \mathbf{I}\right) , \tag{7}$$

where $\mathbf{I}$ is the identity tensor. By introducing the metric coefficients of the first fundamental form, $g_{ij} = \mathbf{g}_i \cdot \mathbf{g}_j$, the Green–Lagrange strain tensor becomes

$$\mathbf{E} = \frac{1}{2}\left(g_{ij} - \mathring{g}_{ij}\right)\mathring{\mathbf{g}}^i \otimes \mathring{\mathbf{g}}^j = E_{ij}\mathring{\mathbf{g}}^i \otimes \mathring{\mathbf{g}}^j . \tag{8}$$

For the continuum shell formulation, the individual strain component E_{ij} can be obtained using the undeformed local covariant vectors and displacement derivatives:

$$E_{ij} = \frac{1}{2}\left(\mathring{\mathbf{g}}_i \cdot \mathbf{u}_{,j} + \mathring{\mathbf{g}}_j \cdot \mathbf{u}_{,i} + \mathbf{u}_{,i} \cdot \mathbf{u}_{,j}\right) , \tag{9}$$

where its variation with respect to $\delta\mathbf{u}$ can be expressed as

$$\delta E_{ij} = \frac{1}{2}\left(\mathring{\mathbf{g}}_i \cdot \delta\mathbf{u}_{,j} + \mathring{\mathbf{g}}_j \cdot \delta\mathbf{u}_{,i} + \delta\mathbf{u}_{,i} \cdot \mathbf{u}_{,j} + \mathbf{u}_{,i} \cdot \delta\mathbf{u}_{,j}\right) = \frac{1}{2}\left(\mathbf{g}_i \cdot \delta\mathbf{u}_{,j} + \mathbf{g}_j \cdot \delta\mathbf{u}_{,i}\right) . \tag{10}$$

In this work, linear elastic material behavior is assumed, corresponding to a St. Venant–Kirchhoff material model. The stress–strain relationship is expressed by $\mathbf{S} = \mathbb{C}\mathbf{E}$, where $\mathbb{C}$ is the fourth-order material elasticity tensor. Note that the above stress and strain tensors are defined under the contravariant coordinates that are not necessarily orthonormal, and thus need to be transformed from the curvilinear system to the element local system:

$$E_{ij}^e = E_{kl}\left(\mathring{\mathbf{g}}^k \cdot \mathbf{e}_i\right)\left(\mathring{\mathbf{g}}^l \cdot \mathbf{e}_j\right) , \tag{11}$$

where E_{ij}^e are the Green–Lagrange strain tensor coefficients with respect to the local Cartesian base vectors $\mathbf{e}_i$ and $\mathbf{e}_j$. More details of the continuum shell formulation can be found in references [82, 89].

Remark 2. The adopted continuum shell formulation can be regarded as a solid that is non-isoparametric in the through-thickness direction (i.e., only isoparametric in the in-plane directions). The geometry is defined by a normal offset of the midsurface, but the displacement field has an arbitrary degree through the thickness. The geometric description in Eq. (1) employs independent discretizations for the reference surface of the shell and for the thickness direction, and this formulation ultimately decouples the numerical integration schemes in the in-plane and out-of-plane directions. While it is not inherently locking-free, this type of solid-like shell formulation also facilitates the introduction of strategies to mitigate locking [110, 111]. Although specific anti-

locking methods have not been introduced in the present continuum shell formulation, Hosseini et al. [82] showed that the use of high-order spline basis functions alleviates locking to some degree. Further discussion on techniques to mitigate locking for solid-like shells can be found in references [112–115].

2.2. Isogeometric composite Kirchhoff–Love shells

For the Kirchhoff–Love shell, both normal and transverse shear strains are neglected, and only the in-plane strain components are considered. The Green–Lagrange strain is assumed to vary linearly through the shell thickness and can be expressed as a combination of membrane and bending strains ($\boldsymbol{\varepsilon}$ and $\boldsymbol{\kappa}$, respectively) of the midsurface. The covariant components of $\mathbf{E}$ can be obtained as

$$E_{\alpha\beta} = \varepsilon_{\alpha\beta} + \xi_3 \kappa_{\alpha\beta} \,, \tag{12}$$

where $\varepsilon_{\alpha\beta}$ and $\kappa_{\alpha\beta}$ are the covariant components of $\boldsymbol{\varepsilon}$ and $\boldsymbol{\kappa}$, respectively, and $\xi_3 \in [-0.5t_h, 0.5t_h]$. Let $\mathbf{r}(\xi_1, \xi_2)$ be the spatial coordinate of the midsurface in the deformed configuration with ξ_1 and ξ_2 being the parametric coordinates of the midsurface, $\mathbf{r} = \mathring{\mathbf{r}} + \mathbf{u}(\xi_3 = 0)$. Let $\mathbf{a}_\alpha$ be the covariant surface base vectors in the deformed configurations, obtained as $\mathbf{a}_\alpha = \mathbf{r}_{,\alpha}$. $\varepsilon_{\alpha\beta}$ and $\kappa_{\alpha\beta}$ are defined as

$$\varepsilon_{\alpha\beta} = \frac{1}{2}\left(\mathbf{a}_\alpha \cdot \mathbf{a}_\beta - \mathring{\mathbf{a}}_\alpha \cdot \mathring{\mathbf{a}}_\beta\right) \,, \tag{13}$$

$$\kappa_{\alpha\beta} = \mathring{\mathbf{a}}_{\alpha,\beta} \cdot \mathring{\mathbf{a}}_3 - \mathbf{a}_{\alpha,\beta} \cdot \mathbf{a}_3 \,, \tag{14}$$

where $\mathring{\mathbf{a}}_i$ are the same as those defined in the previous section, and $\mathbf{a}_3$ is the unit vector normal to the KL shell midsurface in the deformed configuration, given by

$$\mathbf{a}_3 = \frac{\mathbf{a}_1 \times \mathbf{a}_2}{\|\mathbf{a}_1 \times \mathbf{a}_2\|} \,. \tag{15}$$

Remark 3. Note that for the KL shell, an arbitrary point $\mathbf{x}$ in the shell body in the deformed configuration can be described as $\mathbf{x} = \mathbf{r} + \xi_3 \mathbf{a}_3$. The covariant base vectors in the deformed KL shell body can be defined as $\mathbf{g}_i = \mathbf{x}_{,i}$ and expressed as $\mathbf{g}_\alpha = \mathbf{a}_\alpha + \xi_3 \mathbf{a}_{3,\alpha}$ and $\mathbf{g}_3 = \mathbf{a}_3$, which differs from the continuum shell definition in Eq. (5).

Assuming linear elastic material behavior, the internal virtual work for the composite KL shell can be expressed as

$$\delta W^{\text{int}} = \int_{\mathcal{S}_0} \int_{\xi_3} \delta\mathbf{E} : \mathbf{S} \, \mathrm{d}\xi_3 \mathrm{d}\mathcal{S} = \int_{\mathcal{S}_0} \delta\boldsymbol{\varepsilon} : (\mathbb{A}\boldsymbol{\varepsilon} + \mathbb{B}\boldsymbol{\kappa}) \, \mathrm{d}\mathcal{S} + \int_{\mathcal{S}_0} \delta\boldsymbol{\kappa} : (\mathbb{B}\boldsymbol{\varepsilon} + \mathbb{D}\boldsymbol{\kappa}) \, \mathrm{d}\mathcal{S} \,, \tag{16}$$

where $\mathcal{S}_0$ is the shell midsurface in the undeformed configuration, and $\mathbb{A}$, $\mathbb{B}$, and $\mathbb{D}$ are the homogenized membrane, coupling, and bending stiffness tensors, respectively, defined based on the classical laminated plate theory. More details about this formulation can be found in references [62, 65, 116].

2.3. A penalty formulation for blended shell coupling

This section presents a penalty formulation for the coupling of blended KL and continuum shells. The ultimate goal of the blended coupling is threefold: (a) enforce C^0 interface continuity by means of displacement coupling, (b) enforce C^1 interface continuity (i.e., surface tangent continuity) through rotational coupling, and (c) avoid intersection of the surface normal of the KL shell with the continuum shell body at the interface. In addition to the standard displacement and rotational couplings as explained in goals (a) and (b), goal (c) is needed due to the separate through-thickness kinematics in the continuum shell formulation. The proposed formulation is built upon previous work for the penalty coupling of KL shell patches [99] and is applicable not only to blended shell coupling but also to the coupling of pure KL or continuum shells. The method is based on a variational framework and thus works for either matching or non-matching discretizations. Moreover, two patches can be coupled at an arbitrary angle through the inclusion of complementary scalar product penalty terms that enforce the rotational coupling by constraining the surface normal against both the normal and tangential surface directions at the coupling interface. In the following, we consider two patches, Ω^A and Ω^B, that are joined at an interface, $\mathcal{L}$, which is always chosen as the edge of the midsurface of the shell body across various coupling scenarios. It is assumed that Ω^A is a continuum shell patch and Ω^B is a KL shell patch, as illustrated in Figure 1. Note that the covariant base vector $\mathbf{g}_3$ in the deformed configuration of the continuum shell, as defined in Eq. (5), is not a unit vector. However, with a slight abuse of notation in Figure 1 and the following derivation of the penalty formulation, we use $\tilde{\mathbf{g}}_3$ to represent the non-normalized $\mathbf{g}_3$ and redefine $\mathbf{g}_3$ as the normalized vector of $\tilde{\mathbf{g}}_3$, i.e., $\mathbf{g}_3 = \tilde{\mathbf{g}}_3/\|\tilde{\mathbf{g}}_3\|$, for blended coupling at a patch interface.

Augmented by the penalty contribution, the principle of virtual work is re-written in the following form:

$$\delta W = \delta W^{\mathrm{int}} + \delta W^{\mathrm{pd}} + \delta W^{\mathrm{pr}} - \delta W^{\mathrm{ext}} = 0 \,, \tag{17}$$

where δW^{pd} and δW^{pr} are the displacement and rotational penalty contributions, respectively. In order to properly constrain the interfacial continuum shell kinematics in the through-thickness direction, the coupling conditions need to be enforced across the entire interface through an integration over the thickness domain, $\mathcal{T}$. The displacement and rotational penalty terms are enforced with different strategies in order to properly maintain the continuity of the surface normals and surface tangents across the interface. Specifically, the enforcement of displacement continuity is

9
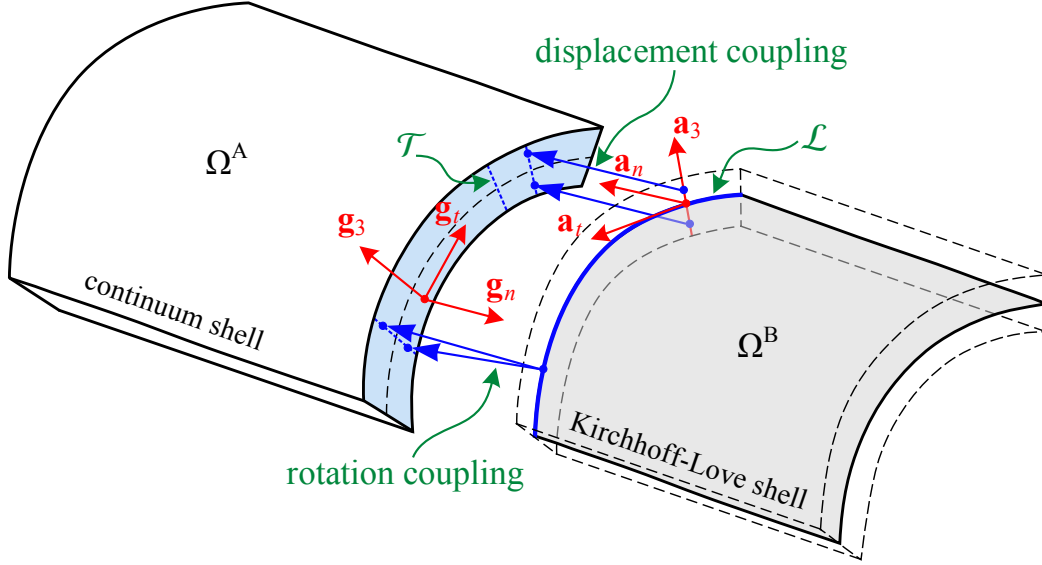
Figure 1: Illustration of the blended coupling interface between a continuum shell and a KL shell. Note that we define $\mathbf{g}_3$ here as the normalized vector of $\tilde{\mathbf{g}}_3$, i.e., $\mathbf{g}_3 = \tilde{\mathbf{g}}_3/\|\tilde{\mathbf{g}}_3\|$, where $\tilde{\mathbf{g}}_3$ is the non-normalized $\mathbf{g}_3$ in Eq. (5).

realized by considering the penalty contribution δW^{pd} in the following manner:

$$\delta W^{\mathrm{pd}} = \int_{\mathcal{L}} \int_{\mathcal{T}} \alpha_{\mathrm{d}} \left(\mathbf{u}^{\mathrm{A}} - \mathbf{u}^{\mathrm{B}} \right) \cdot \left(\delta \mathbf{u}^{\mathrm{A}} - \delta \mathbf{u}^{\mathrm{B}} \right) \mathrm{d}\mathcal{T} \mathrm{d}\mathcal{L} \,, \tag{18}$$

where α_{d} is the displacement penalty parameter that will be defined later, and $\mathbf{u}^{\mathrm{A}}$ and $\mathbf{u}^{\mathrm{B}}$ represent the displacements at the corresponding through-thickness locations on Ω^{A} and Ω^{B}, respectively. Recall that the off-the-midsurface position vector in a shell body can be described using Eq. (1), and thus $\mathbf{u}^{\mathrm{B}}$ on the KL shell side can be conveniently obtained by subtracting the reference position vector $\mathring{\mathbf{x}}^{\mathrm{B}}$ from the current position vector $\mathbf{x}^{\mathrm{B}}$. Eq. (18) dictates that a large penalty energy will be introduced into the system provided that there are relative motions between any two corresponding through-thickness points on Ω^{A} and Ω^{B} along the penalty curve $\mathcal{L}$. Note that, due to the separate through-thickness kinematics in the continuum shell formulation, the interface tangent in the through-thickness direction, $\mathbf{g}_3^{\mathrm{tan}}$, and the continuum shell surface normal, $\mathbf{g}_3$, can be different in the deformed configuration, as illustrated in Figure 2. By enforcing the displacement coupling over the entire interface between continuum and KL shell patches, as outlined in goal (c) for blended shell coupling, this type of continuum shell deformation is eliminated for the blended interface. This constraint accounts for the KL shell kinematics by maintaining the continuity between the interface tangent in the through-thickness direction on the continuum shell side and the surface normal on the KL shell side.

10
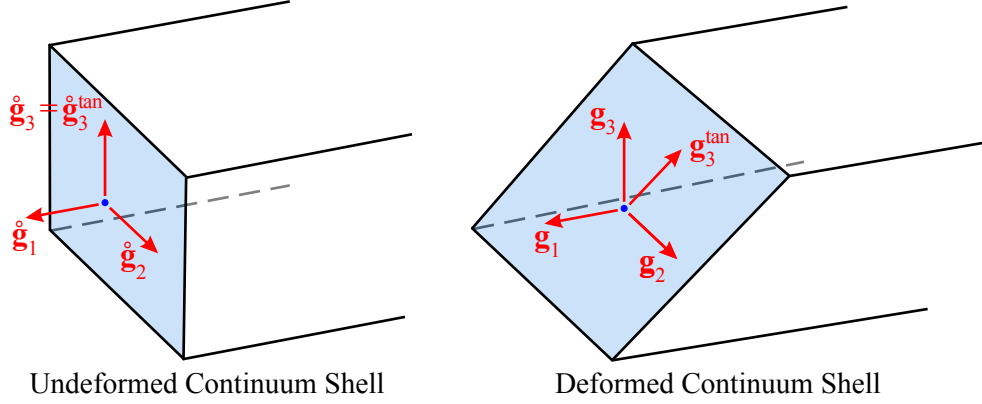
Figure 2: Example of possible interface deformation at the edge of the continuum shell body. The interface tangent in the through-thickness direction, $\mathbf{g}_3^{\mathrm{tan}}$, is shown in the undeformed and deformed configurations. When coupling continuum and KL shells at this interface, the alignment of $\mathbf{g}_3^{\mathrm{tan}}$ and the surface normal, $\mathbf{g}_3$, is enforced with the through-thickness displacement constraint, which prevents this type of interface deformation. Note that such deformation can occur at a coupling interface between two continuum shells.

The inter-patch rotational continuity can be achieved by expanding the rotational penalty work δW^{pr} as:

$$
\begin{aligned}
\delta W^{\mathrm{pr}} = \int_{\mathcal{L}} \int_{\mathcal{T}} \alpha_{\mathrm{r}} \Big(& \big(\mathbf{g}_3^{\mathrm{A}} \cdot \mathbf{a}_3^{\mathrm{B}} - \mathring{\mathbf{g}}_3^{\mathrm{A}} \cdot \mathring{\mathbf{a}}_3^{\mathrm{B}} \big) \big(\delta \mathbf{g}_3^{\mathrm{A}} \cdot \mathbf{a}_3^{\mathrm{B}} + \mathbf{g}_3^{\mathrm{A}} \cdot \delta \mathbf{a}_3^{\mathrm{B}} \big) \\
& + \big(\mathbf{g}_n^{\mathrm{A}} \cdot \mathbf{a}_3^{\mathrm{B}} - \mathring{\mathbf{g}}_n^{\mathrm{A}} \cdot \mathring{\mathbf{a}}_3^{\mathrm{B}} \big) \big(\delta \mathbf{g}_n^{\mathrm{A}} \cdot \mathbf{a}_3^{\mathrm{B}} + \mathbf{g}_n^{\mathrm{A}} \cdot \delta \mathbf{a}_3^{\mathrm{B}} \big) \Big) \mathrm{d}\mathcal{T} \mathrm{d}\mathcal{L}
\end{aligned}
\tag{19}
$$

where α_{r} is the rotational penalty parameter that will be discussed later with the displacement penalty parameter α_{d}, and $\mathbf{g}_n^{\mathrm{A}}$ is the in-plane covariant unit vector normal to the penalty plane $\mathcal{L} \times \mathcal{T}$ as illustrated in Figure 1. Introducing the in-plane vector tangent to the penalty plane of patch Ω^{A}, $\tilde{\mathbf{g}}_t^{\mathrm{A}} = \mathbf{x}_{,t}^{\mathrm{A}}$, $\mathbf{g}_n^{\mathrm{A}}$ can be uniquely determined by $\mathbf{g}_n^{\mathrm{A}} = \mathbf{g}_t^{\mathrm{A}} \times \mathbf{g}_3^{\mathrm{A}}$, where $\mathbf{g}_t^{\mathrm{A}}$ is the normalized vector of $\tilde{\mathbf{g}}_t^{\mathrm{A}}$, i.e., $\mathbf{g}_t^{\mathrm{A}} = \tilde{\mathbf{g}}_t^{\mathrm{A}} / \|\tilde{\mathbf{g}}_t^{\mathrm{A}}\|$, and $\mathbf{g}_3^{\mathrm{A}}$ is a unit vector normalized analogously. Similar to the enforcement of rotational continuity for the coupling of KL shells [99], the present formulation for the coupling of blended shells considers two sets of interfacial unit vectors as the criterion for introducing the rotational penalty energy. This consideration accounts for the fact that the scalar product of two parallel unit vectors vanishes in the variational form for two patches that are tangent at their interface, whereas the scalar product of two orthonormal vectors vanishes for two patches that are joined at a 90° angle. Therefore, the inclusion of both terms is needed in order to ensure rotational continuity at an arbitrary joining angle.

Once the penalty-augmented virtual work is derived, linearization of the equations is necessary to obtain the internal force and the tangent stiffness tensors. In the following equations, r and s are the indices for the total degrees of freedom of the system, and the partial derivatives with respect to the discrete nodal displacements, u_r and u_s, are denoted as $(\cdot)_{,r}$ and $(\cdot)_{,s}$, respectively. By taking

first-order derivatives of Eqs. ([18]) and ([19]) with respect to the displacement variables, we arrive at the internal force contributions of the penalty work in the following form:

$$\frac{\partial W^{\mathrm{pd}}}{\partial u_r} = \int_{\mathcal{L}} \int_{\mathcal{T}} \alpha_{\mathrm{d}} \left(\mathbf{u}^{\mathrm{A}} - \mathbf{u}^{\mathrm{B}} \right) \cdot \left(\mathbf{u}^{\mathrm{A}}_{,r} - \mathbf{u}^{\mathrm{B}}_{,r} \right) \mathrm{d}\mathcal{T} \mathrm{d}\mathcal{L} , \tag{20}$$

$$\frac{\partial W^{\mathrm{pr}}}{\partial u_r} = \int_{\mathcal{L}} \int_{\mathcal{T}} \alpha_{\mathrm{r}} \left(\left(\mathbf{g}^{\mathrm{A}}_3 \cdot \mathbf{a}^{\mathrm{B}}_3 - \mathring{\mathbf{g}}^{\mathrm{A}}_3 \cdot \mathring{\mathbf{a}}^{\mathrm{B}}_3 \right) \left(\mathbf{g}^{\mathrm{A}}_{3,r} \cdot \mathbf{a}^{\mathrm{B}}_3 + \mathbf{g}^{\mathrm{A}}_3 \cdot \mathbf{a}^{\mathrm{B}}_{3,r} \right) \right.$$
$$\left. + \left(\mathbf{g}^{\mathrm{A}}_n \cdot \mathbf{a}^{\mathrm{B}}_3 - \mathring{\mathbf{g}}^{\mathrm{A}}_n \cdot \mathring{\mathbf{a}}^{\mathrm{B}}_3 \right) \left(\mathbf{g}^{\mathrm{A}}_{n,r} \cdot \mathbf{a}^{\mathrm{B}}_3 + \mathbf{g}^{\mathrm{A}}_n \cdot \mathbf{a}^{\mathrm{B}}_{3,r} \right) \right) \mathrm{d}\mathcal{T} \mathrm{d}\mathcal{L} . \tag{21}$$

Through further taking derivatives with respect to the field variables, the penalty stiffness contribution is revealed:

$$\frac{\partial^2 W^{\mathrm{pd}}}{\partial u_r \partial u_s} = \int_{\mathcal{L}} \int_{\mathcal{T}} \alpha_{\mathrm{d}} \left(\left(\mathbf{u}^{\mathrm{A}}_{,s} - \mathbf{u}^{\mathrm{B}}_{,s} \right) \cdot \left(\mathbf{u}^{\mathrm{A}}_{,r} - \mathbf{u}^{\mathrm{B}}_{,r} \right) - \left(\mathbf{u}^{\mathrm{A}} - \mathbf{u}^{\mathrm{B}} \right) \cdot \mathbf{u}^{\mathrm{B}}_{,rs} \right) \mathrm{d}\mathcal{T} \mathrm{d}\mathcal{L} , \tag{22}$$

$$\frac{\partial^2 W^{\mathrm{pr}}}{\partial u_r \partial u_s} = \int_{\mathcal{L}} \int_{\mathcal{T}} \alpha_{\mathrm{r}} \left(\left(\mathbf{g}^{\mathrm{A}}_3 \cdot \mathbf{a}^{\mathrm{B}}_3 - \mathring{\mathbf{g}}^{\mathrm{A}}_3 \cdot \mathring{\mathbf{a}}^{\mathrm{B}}_3 \right) \left(\mathbf{g}^{\mathrm{A}}_{3,rs} \cdot \mathbf{a}^{\mathrm{B}}_3 + \mathbf{g}^{\mathrm{A}}_{3,r} \cdot \mathbf{a}^{\mathrm{B}}_{3,s} + \mathbf{g}^{\mathrm{A}}_{3,s} \cdot \mathbf{a}^{\mathrm{B}}_{3,r} + \mathbf{g}^{\mathrm{A}}_3 \cdot \mathbf{a}^{\mathrm{B}}_{3,rs} \right) \right.$$
$$+ \left(\mathbf{g}^{\mathrm{A}}_{3,s} \cdot \mathbf{a}^{\mathrm{B}}_3 + \mathbf{g}^{\mathrm{A}}_3 \cdot \mathbf{a}^{\mathrm{B}}_{3,s} \right) \left(\mathbf{g}^{\mathrm{A}}_{3,r} \cdot \mathbf{a}^{\mathrm{B}}_3 + \mathbf{g}^{\mathrm{A}}_3 \cdot \mathbf{a}^{\mathrm{B}}_{3,r} \right)$$
$$+ \left(\mathbf{g}^{\mathrm{A}}_n \cdot \mathbf{a}^{\mathrm{B}}_3 - \mathring{\mathbf{g}}^{\mathrm{A}}_n \cdot \mathring{\mathbf{a}}^{\mathrm{B}}_3 \right) \left(\mathbf{g}^{\mathrm{A}}_{n,rs} \cdot \mathbf{a}^{\mathrm{B}}_3 + \mathbf{g}^{\mathrm{A}}_{n,r} \cdot \mathbf{a}^{\mathrm{B}}_{3,s} + \mathbf{g}^{\mathrm{A}}_{n,s} \cdot \mathbf{a}^{\mathrm{B}}_{3,r} + \mathbf{g}^{\mathrm{A}}_n \cdot \mathbf{a}^{\mathrm{B}}_{3,rs} \right)$$
$$\left. + \left(\mathbf{g}^{\mathrm{A}}_{n,s} \cdot \mathbf{a}^{\mathrm{B}}_3 + \mathbf{g}^{\mathrm{A}}_n \cdot \mathbf{a}^{\mathrm{B}}_{3,s} \right) \left(\mathbf{g}^{\mathrm{A}}_{n,r} \cdot \mathbf{a}^{\mathrm{B}}_3 + \mathbf{g}^{\mathrm{A}}_n \cdot \mathbf{a}^{\mathrm{B}}_{3,r} \right) \right) \mathrm{d}\mathcal{T} \mathrm{d}\mathcal{L} . \tag{23}$$

In the above equations, the variations of the displacement vector with respect to u_r and u_s on the continuum shell side can be directly obtained using $\mathbf{u}^{\mathrm{A}}_{,r} = R^a N^a \hat{\mathbf{e}}_i$ and $\mathbf{u}^{\mathrm{A}}_{,rs} = \mathbf{0}$, where i and a indicate the ith displacement component of control point a, R^a and N^a are the associated in-plane NURBS and through-thickness B-spline basis functions, respectively, and $\hat{\mathbf{e}}_i$ is the global Cartesian basis. This is in contrast to the KL shell side, where the variations of the displacement vector are obtained as $\mathbf{u}^{\mathrm{B}}_{,r} = \mathbf{r}^{\mathrm{B}}_{,r} + \xi_3 \mathbf{a}^{\mathrm{B}}_{3,r}$ and $\mathbf{u}^{\mathrm{B}}_{,rs} = \xi_3 \mathbf{a}^{\mathrm{B}}_{3,rs}$. Note that, in the standard KL shell formulation, the derivatives with respect to $\xi_3 \mathbf{a}_3$ are not included in $\mathbf{u}_{,r}$ and $\mathbf{u}_{,rs}$, because the final form of the internal virtual work for KL shells is formulated based on the midsurface on which $\xi_3 = 0$ (see Eq. ([16])). However, since the proposed displacement coupling is carried out through an integration over the thickness domain $\mathcal{T}$, these derivatives are generally nonzero and thus need to be considered. For continuum shells, the evaluation of the first and second derivatives of $\mathbf{g}_3$ and $\mathbf{g}_n$ are also necessary, which can be obtained as follows:

$$\mathbf{g}_{(\cdot),r} = \frac{1}{\|\tilde{\mathbf{g}}_{(\cdot)}\|} \left(\tilde{\mathbf{g}}_{(\cdot),r} - \left(\mathbf{g}_{(\cdot)} \cdot \tilde{\mathbf{g}}_{(\cdot),r} \right) \mathbf{g}_{(\cdot)} \right) , \tag{24}$$

$$\mathbf{g}_{n,r} = \mathbf{g}_{t,r} \times \mathbf{g}_3 + \mathbf{g}_t \times \mathbf{g}_{3,r} , \tag{25}$$

and

$$\mathbf{g}_{(\cdot),rs} = -\frac{1}{\|\tilde{\mathbf{g}}_{(\cdot)}\|} \left(\left(\mathbf{g}_{(\cdot),s} \cdot \tilde{\mathbf{g}}_{(\cdot),r} \right) \mathbf{g}_{(\cdot)} + \left(\mathbf{g}_{(\cdot)} \cdot \tilde{\mathbf{g}}_{(\cdot),s} \right) \mathbf{g}_{(\cdot),r} + \left(\mathbf{g}_{(\cdot)} \cdot \tilde{\mathbf{g}}_{(\cdot),r} \right) \mathbf{g}_{(\cdot),s} \right) , \qquad (26)$$

$$\mathbf{g}_{n,rs} = \mathbf{g}_{t,rs} \times \mathbf{g}_3 + \mathbf{g}_{t,r} \times \mathbf{g}_{3,s} + \mathbf{g}_{t,s} \times \mathbf{g}_{3,r} + \mathbf{g}_t \times \mathbf{g}_{3,rs} , \qquad (27)$$

where $(\cdot)$ represents 3 or t, and $\mathbf{g}_{(\cdot),s}$ and $\mathbf{g}_{n,s}$ are defined analogously to Eqs. (24) and (25), respectively, with r replaced by s. For KL shells, $\mathbf{a}_{3,r}$, $\mathbf{a}_{3,s}$, and $\mathbf{a}_{3,rs}$ in Eqs. (21)–(23) are defined similarly to Eqs. (24) and (26) with $\mathbf{g}$ replaced by $\mathbf{a}$. Additional details regarding the derivation of the variables used in these expressions can be found in Kiendl et al. [40, Appendix C].

Remark 4. The formulation can be further simplified when coupling occurs at patch edges, where $\tilde{\mathbf{g}}_t$ simply becomes $\mathbf{g}_1$ or $\mathbf{g}_2$, depending on the parametric edges that are coupled. The present formulation is also applicable to the coupling at a trimming curve, where $\tilde{\mathbf{g}}_t$ can be obtained by projecting the trimming curve to the patch and evaluating the tangent vector at the corresponding location. Finally, the above formulation can also be applied to weakly impose boundary and symmetry conditions; additional details can be found in Herrema et al. [99].

Remark 5. In the case of two KL shell patches that are coupled at their midsurfaces, $\mathbf{g}_n^{\mathrm{A}}$, $\mathbf{g}_t^{\mathrm{A}}$, and $\mathbf{g}_3^{\mathrm{A}}$ and their undeformed versions degenerate to the corresponding unit vectors on the midsurface, and all the displacements and their derivatives are evaluated at the midsurface. In the case of pure continuum shell coupling over the shell interfaces, the surface vectors $\mathbf{a}_n^{\mathrm{B}}$, $\mathbf{a}_t^{\mathrm{B}}$, and $\mathbf{a}_3^{\mathrm{B}}$ and their undeformed versions are replaced by the corresponding shell body vectors $\mathbf{g}_n^{\mathrm{B}}$, $\mathbf{g}_t^{\mathrm{B}}$, and $\mathbf{g}_3^{\mathrm{B}}$ and their undeformed versions.

2.4. Element-wise evaluation of penalty parameters

Standard penalty-based methods are notorious for their troublesome and empirical selection of the penalty parameter: the imposed constraints cannot be sufficiently satisfied if the penalty parameter is too low, whereas the system becomes ill-conditioned with an overly high penalty parameter. Thus, this section is dedicated to eliminating this bottleneck and providing a single and universal selection of the penalty parameter that is applicable to both displacement and rotational continuity enforcement irrespective of the problem configuration. Specifically, the present work adopts a strategy for selecting the penalty parameters that is similar to the selection approach for coupling pure KL shells [99]. Note that, unlike the original form, the division of the penalty parameters α_{d} and α_{r} by the shell thickness t_h is needed due to the integration over the thickness domain. In the case of isotropic materials, the displacement penalty parameter α_{d} and the rotational

penalty parameter α_r are determined as:

$$\alpha_d = \alpha \frac{E}{h\,(1 - v^2)} \ , \quad \alpha_r = \alpha \frac{E\,t_h^2}{12\,h\,(1 - v^2)} \ , \tag{28}$$

whereas, in the case of composite materials, these expressions become:

$$\alpha_d = \alpha \frac{\max_{i,j}\left(\mathbb{A}_{ij}\right)}{h\,t_h} \ , \quad \alpha_r = \alpha \frac{\max_{i,j}\left(\mathbb{D}_{ij}\right)}{h\,t_h} \ . \tag{29}$$

In the above, E is the Young's modulus, v is the Poisson's ratio, t_h is the shell thickness, and $\mathbb{A}_{ij}$ and $\mathbb{D}_{ij}$ are the membrane and bending stiffness components of the composite, respectively, defined based on the classical laminated plate theory. In this work, the element size parameter h is determined by averaging the corresponding element lengths on the two patches along the local element direction most parallel to the penalty curve. The directional element length h^e on each patch is extracted from the in-plane element metric tensor $\mathbf{G}$:

$$\mathbf{G} = \frac{\partial \boldsymbol{\zeta}^T}{\partial \bar{\mathbf{x}}} \frac{\partial \boldsymbol{\zeta}}{\partial \bar{\mathbf{x}}} \ , \tag{30}$$

$$h^e = 2\,(\mathbf{r} \cdot \mathbf{G}\,\mathbf{r})^{-\frac{1}{2}} \ , \tag{31}$$

where $\bar{\mathbf{x}}$ and $\boldsymbol{\zeta} \in [-1, 1] \times [-1, 1]$ are the in-plane element physical coordinates and integration parametric coordinates, respectively, and $\mathbf{r}$ is a unit vector representing a direction in the physical space. Other approaches to evaluate the element size can be found in references [117, 118].

In Eqs. (28) and (29), both the displacement and the rotational penalty parameters are determined by a single dimensionless value of α. To account for various problem configurations, the parameters are defined to be dimensionally consistent and are specifically scaled by the material properties, shell thickness, and element size. As shown later in Section 3, this single penalty parameter can be chosen universally regardless of the problem setup.

Remark 6. Eqs. (28) and (29) assume that the material properties between coupled patches are continuous. Additional considerations for selecting the penalty parameter at a discontinuous material interface should be included where necessary [99]. When coupling patches with different shell thicknesses, we recommend defining the thickness domain $\mathcal{T}$ and t_h based on the thinner patch.

Remark 7. Another primary advantage of using the continuum shells specified in this work arises from the consistent KL and continuum shell formulations, which have similar curvilinear definitions of the in-plane reference surfaces and both only require modeling the reference surface geometry. These similarities allow efficient blended coupling and direct replacement of KL shell patches with continuum shells at any location on the geometry. This accessibility facilitates evalu-

ating either type of stress anywhere on the geometry by interchanging the KL and continuum shells without having to introduce a specific solid model.

3. Benchmark examples

A number of benchmark examples with a variety of problem setups are employed in this section to demonstrate the applicability and flexibility of the present method, including linear and nonlinear analyses, matching and non-matching discretizations, and isotropic and composite materials. The proper range of the dimensionless penalty parameter α is also studied, and the recommendation of a universal value is given. If not otherwise stated, bicubic NURBS are employed for the representation of the in-plane geometries, and quadratic B-splines are adopted for the description of the through-thickness kinematics of the continuum shells. Note that, while the use of one quadratic element in the thickness direction is generally sufficient for the analysis of isotropic thin-shell structures with simple loading conditions, h- or p-refinement through the thickness may become necessary to capture the accurate 3D stress distribution in more complex settings. Additionally, when modeling composite materials using continuum shells, knot repetition is performed in the thickness direction to create a C^0 dissimilar material interface and a discretization of one thickness element per layer is used.

3.1. Scordelis–Lo roof

The benchmark Scordelis–Lo roof model employed here is intended to verify the geometrically linear response of the blended coupling approach and to test its robustness in complex strain states. The problem setup is illustrated in Figure 3, where the ends of the roof are supported by rigid diaphragms and the straight edges are left free. The roof is subjected to a uniform gravitational load of 90 per unit area applied to the midsurface of the model, and the solution is quantified by the maximum z deflection at the free edges. Due to symmetry, only a quarter of the roof is modeled. The thickness of the shell is $t_h = 0.25$, and the material properties are $E = 4.32 \times 10^8$ and $\nu = 0.0$. The deformed shape of the quarter roof model is shown in Figure 3.

The quarter roof model is described using four patches with both matching and non-matching discretizations, and the initial meshes are shown in Figure 4, where the two patches highlighted with thicker blue edges are modeled using continuum shells and the other two patches are modeled using KL shells. To explore the effective range of the penalty coefficient α, the analysis is repeated with a range of α values. The material properties and shell thickness are also modified in order to demonstrate the robustness of the universal choice of α. These analyses are performed on the meshes shown in Figure 4 with four additional levels of h-refinement. As shown later, converged solutions can be obtained using this level of h-refinement.

15
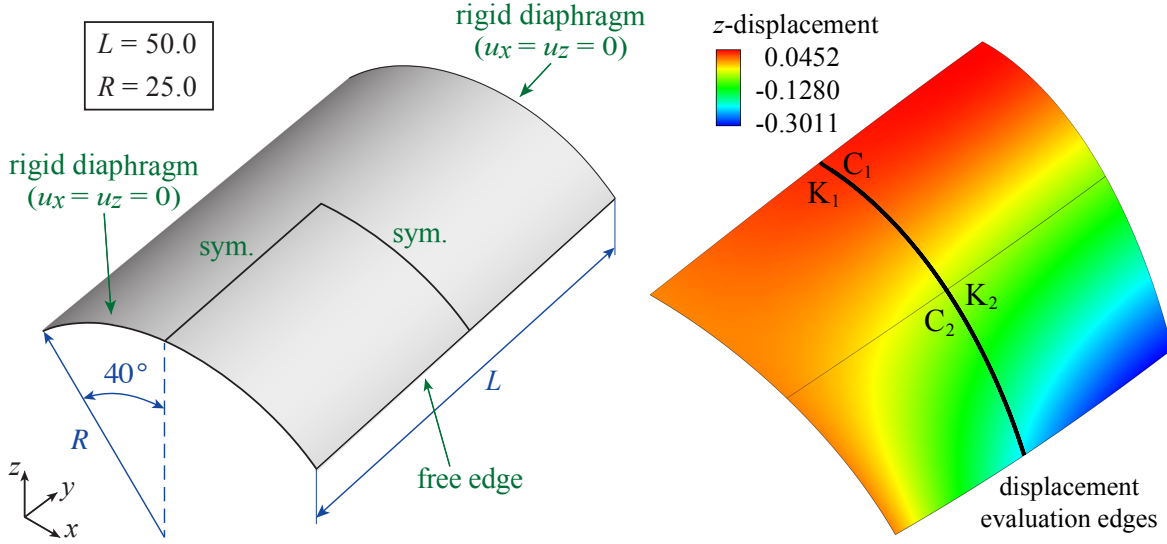
Figure 3: Scordelis–Lo roof model setup and the deformation of a quarter of the model (displayed using the non-matching mesh case and scaled by a factor of 20 for visualization).
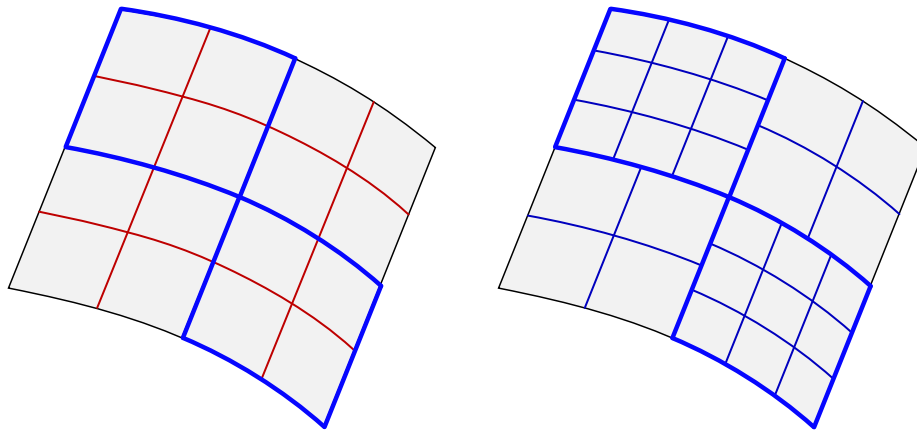
Figure 4: Initial discretizations for the matching (left) and non-matching (right) quarter roof model. Black lines indicate patch boundaries and the thicker blue lines indicate patches modeled using continuum shells.

The results of the parametric studies on α are plotted in Figure 5. The displacements in Figure 5a are normalized against the converged solution of $u_z = -0.301106$ for both the matching and non-matching cases. Based on reported solutions from the literature [93, 99], which are between -0.3005925 and -0.3024, the converged solution from the blended shell analysis is considered accurate. As one can observe in Figure 5a, the solutions of both the matching and non-matching discretizations indicate consistency in the effective range of α values for which the blended coupling method yields accurate solutions. Specifically, the solution is generally accurate when the penalty coefficient α falls in the range of 10^1 to 10^6. The solution deviates from the converged solution as α becomes too large or too small. This is expected, as the coupling constraints are not sufficiently enforced with an overly small penalty coefficient, and the system becomes ill-conditioned

16

(a) $E = 4.32 \times 10^8$, $t_h = 0.25$ (b) $E = 4.32 \times 10^{12}$, $t_h = 0.25$ (c) $E = 4.32 \times 10^8$, $t_h = 0.025$
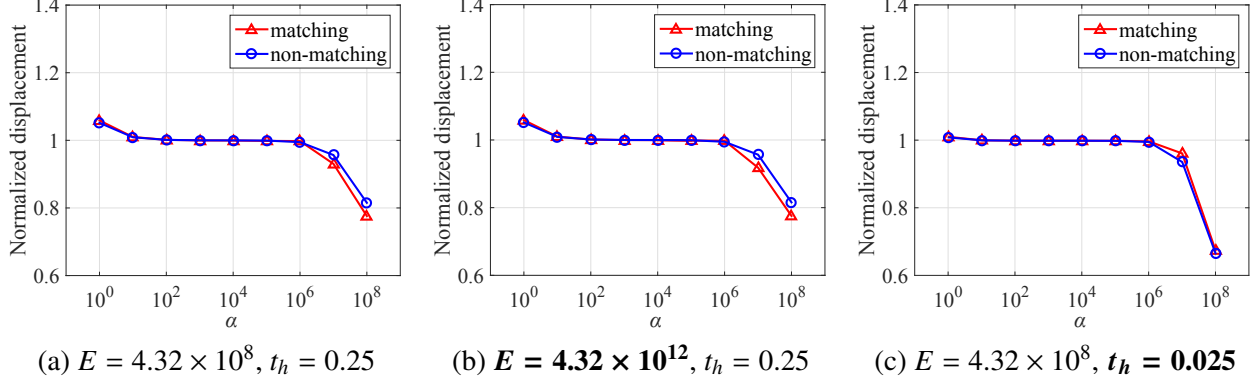
Figure 5: Maximum $-z$-displacement of the quarter roof model, normalized with respect to the converged solution, for a wide range of the penalty coefficient α for both matching and non-matching discretizations and various combinations of problem-specific variables.

with an overly high selection of the penalty coefficient. In order to demonstrate the robustness of the proposed method, some problem-specific variables of the model are further modified. As shown in Figure 5b and Figure 5c, the solutions are obtained with a modified Young's modulus of $E = 4.32 \times 10^{12}$ (instead of the original $E = 4.32 \times 10^8$) and shell thickness of $t_h = 0.025$ (instead of the original $t_h = 0.25$), respectively. Note that the displayed solutions are normalized by the converged solution of $u_z = -3.01107 \times 10^{-5}$ in the first case and $u_z = -32.0123$ in the second case. Accurate solutions for all problem setups are achieved using the same range of α. This successfully circumvents the problematic shifts in penalty coefficient values in traditional penalty-based methods where one has to estimate the problem-specific penalty coefficient in an empirical manner. As such, a value of $\alpha = 10^3$ is recommended, which will also be demonstrated as an effective value in other numerical examples.

To further examine the effectiveness of the patch coupling across the penalty curves, the displacement solutions, computed using the recommended value of $\alpha = 10^3$, are evaluated on the patch boundaries indicated on the deformed configuration of the quarter roof in Figure 3. As shown in Figure 6, the displacement components in all three directions are consistent across the patch boundaries and at the corner location where all four patches meet. These results demonstrate the effectiveness of the proposed method in enforcing the displacement and rotational continuities across the patch boundaries, as demonstrated by the tangential smoothness across the penalty curves perpendicular to the highlighted displacement evaluation edges.

Using the recommended value of $\alpha = 10^3$, a convergence analysis is carried out under uniform h-refinement based on the initial meshes shown in Figure 4. The results displayed in Figure 7 demonstrate excellent convergence in both the matching and non-matching cases.
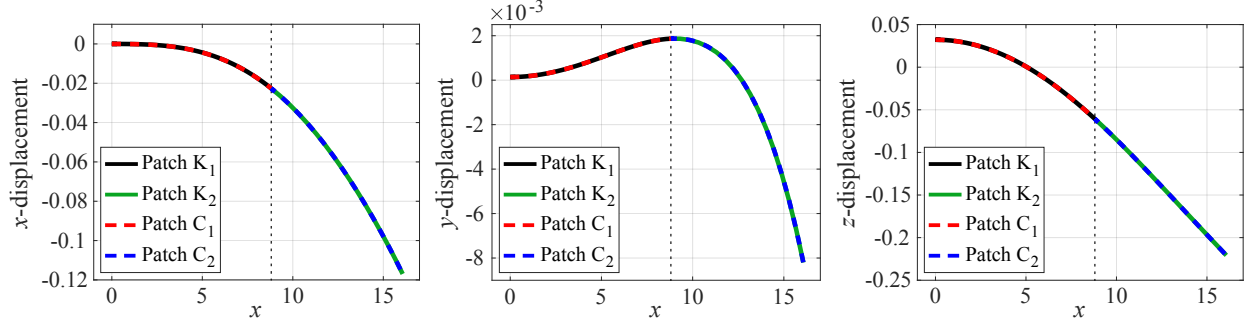
Figure 6: Displacement solution comparison across the boundaries of the specified patches, labeled as C_1, C_2, K_1, and K_2, indicated on the deformed configuration of the quarter roof model in Figure 3. The vertical dotted line indicates the patch division, and the labels "C" and "K" indicate a continuum or a KL shell patch, respectively.
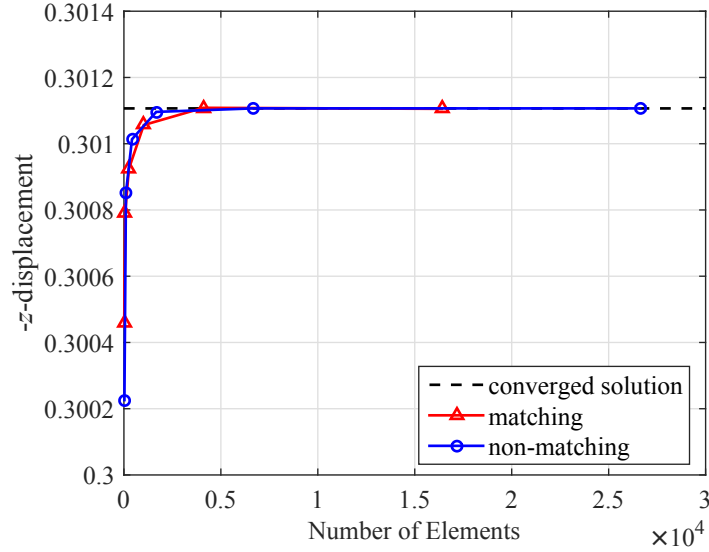
Figure 7: Maximum $-z$-displacement of the quarter roof model under h-refinement for the proposed blended coupling approach with $\alpha = 10^3$.

3.2. Nonlinear slit annular plate

The second numerical example considered here is a slit annular plate model that is fixed at one end and subjected to a lifting line load at the other end. This example is intended to verify the nonlinear performance of the proposed blended shell method. For this problem, a reference solution is available in Sze et al. [119]. The problem setup and the final deformed shape are illustrated in Figure 8, where the vertical displacements at points A and B at the loaded end are monitored and compared with the reference solution. The model has a thickness of $t_h = 0.03$, and the material is isotropic with a Young's modulus of $E = 2.1 \times 10^7$ and a Poisson's ratio of $\nu = 0.0$.

As demonstrated in Figure 9, the problem is modeled with a total of six patches, where the patches with thicker blue edges are modeled using continuum shells, and the rest of the patches
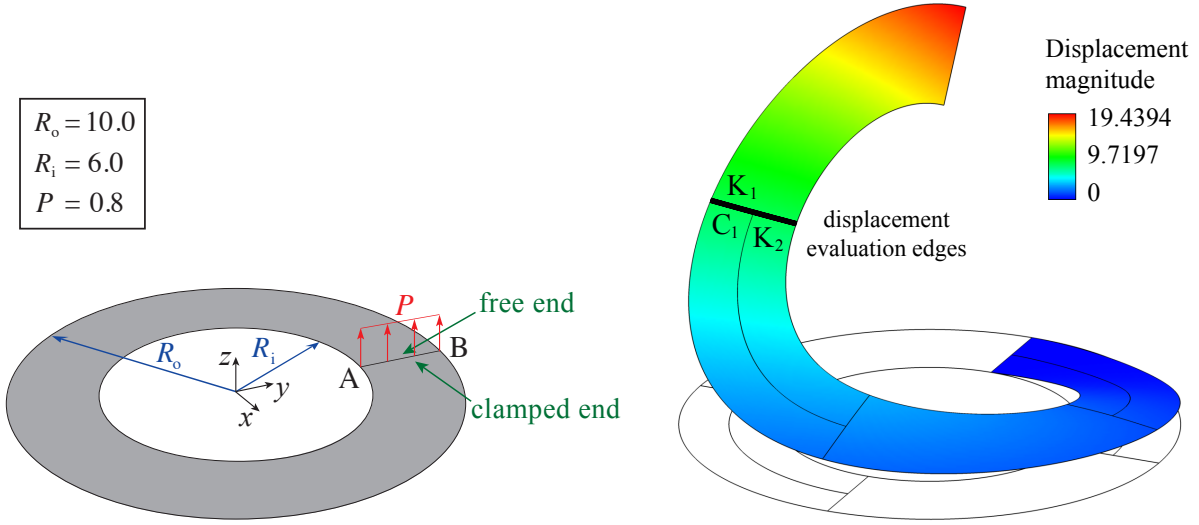
Figure 8: Nonlinear slit annular plate problem setup and the deformed configuration with the non-matching mesh.
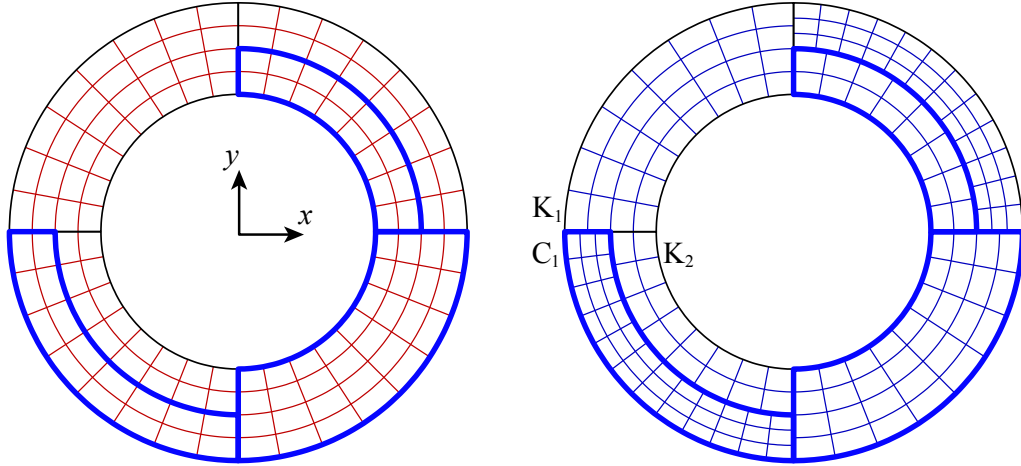
Figure 9: Meshes for the matching (left) and non-matching (right) cases of the nonlinear slit annular plate. Black lines indicate patch boundaries and the thicker blue lines indicate continuum shell patches.

are modeled using KL shells. Both matching and non-matching discretizations are considered. In order to fully test the blended coupling behavior in the nonlinear setting, the blending is devised such that it covers all possible coupling scenarios for this problem, including the blended coupling in the transverse and radial directions. Note that Figure 9 corresponds to the initial coarse meshes of the problem, and a mesh refinement study is also performed to obtain a converged solution. For the convergence analysis, the recommended value of $\alpha = 10^3$ for the penalty parameter is employed. The final vertical displacement at point B using various meshes is plotted in Figure 10, where convergence is clearly observed after two levels of h-refinement in both the matching and non-matching cases. Therefore, these levels of refinements are used in the subsequent sensitivity study of α.
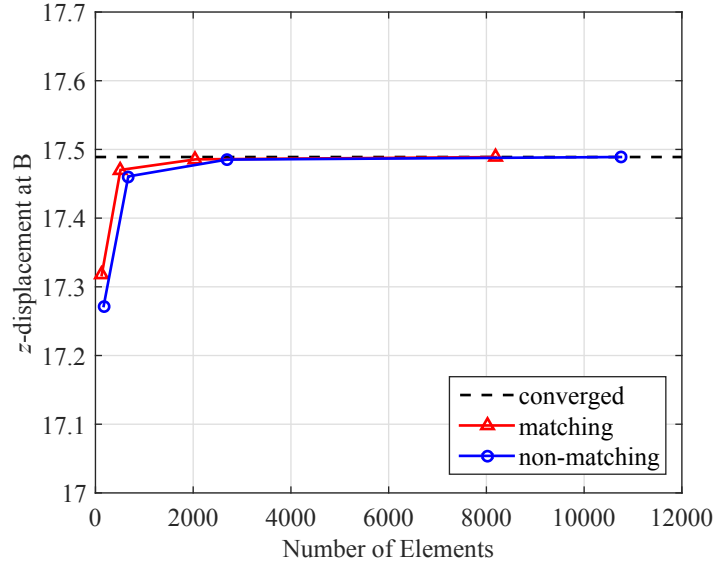
Figure 10: Vertical displacement at point B of the slit annular plate under h-refinement for both matching and non-matching configurations.
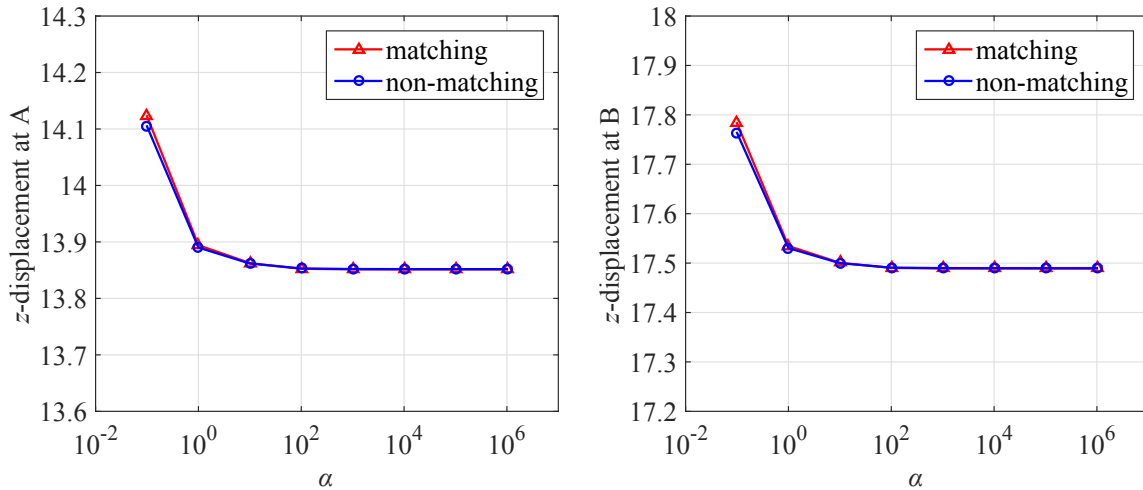
Figure 11: Final vertical displacements at points A and B of the slit annular plate problem for a wide range of α selections.

The vertical displacements at A and B are plotted in Figure 11 against a wide range of α values. A stabilized solution is observed as α increases from 10^2 to 10^6. For α smaller than 10^2, the penalty contribution is not large enough to accurately maintain the rotational continuity, whereas, for α greater than 10^6, the solution becomes difficult to converge due to the ill-conditioning of the system matrices. Nevertheless, similar conclusions can be drawn from this example: the solutions remain accurate for a wide range of α selections (i.e., from 10^2 to 10^6), and the recommended value of $\alpha = 10^3$ still holds.

The displacement solutions across the patch boundaries, indicated by the displacement evalua-
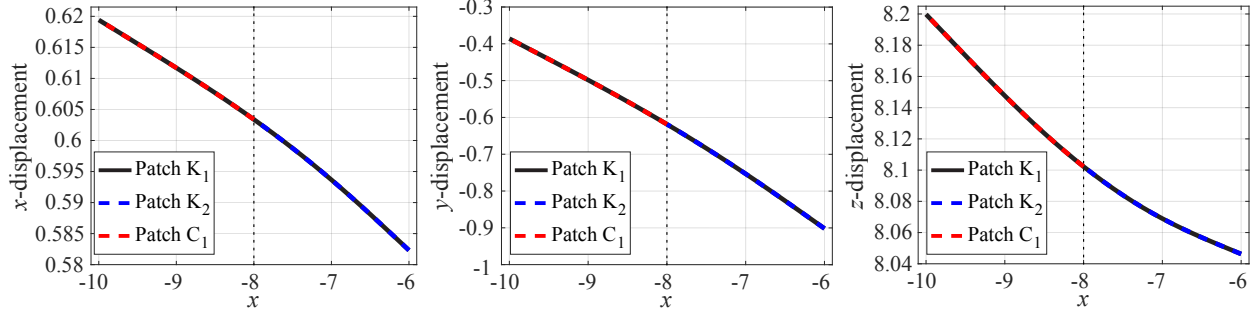
Figure 12: Displacement solution comparison across the boundaries of the specified patches, labeled as C_1, K_1, and K_2, indicated on the deformed configuration of the annular plate model in Figure 8. The vertical dotted line indicates the patch division, and the labels "C" and "K" indicate a continuum or a KL shell patch, respectively.
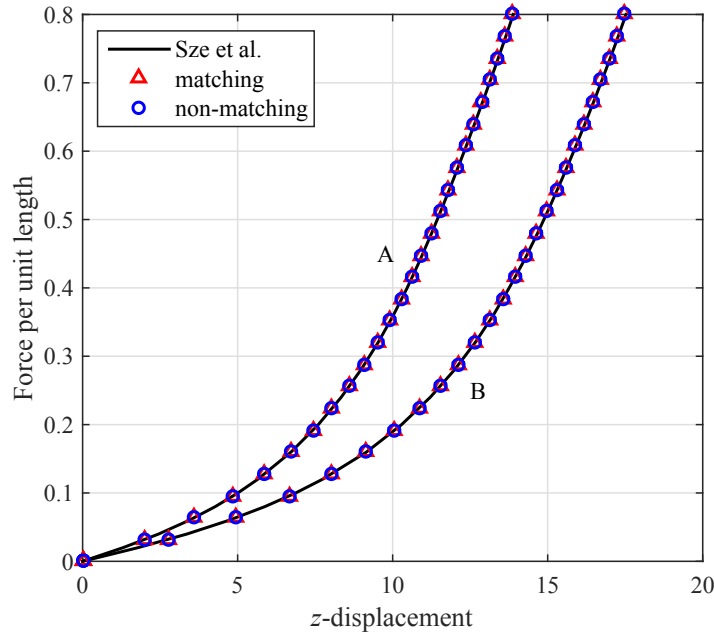
Figure 13: Comparison of the obtained vertical displacement trajectory at points A and B with $\alpha = 10^3$ against the reference solution.

tion edges in Figure 8, are evaluated in Figure 12 using $\alpha = 10^3$. Similar to the previous findings in the roof problem, the proposed method effectively enforces the displacement and rotational continuities across the penalty curves, which demonstrates the overall effectiveness of the blended shell approach for nonlinear analysis.

Finally, Figure 13 shows the comparison between the obtained vertical deflection trajectory at points A and B with $\alpha = 10^3$ and the reference solutions [119]. Excellent agreement is observed for both the matching and non-matching cases.

21
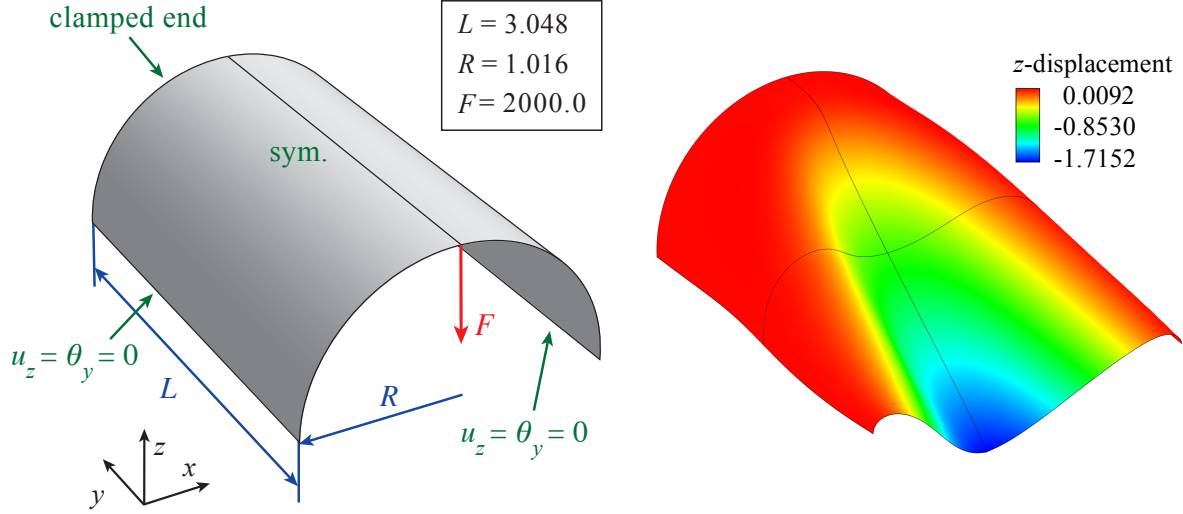
Figure 14: Nonlinear pinched semi-cylinder problem setup and the deformed configuration of the isotropic case plotted using the non-matching mesh.
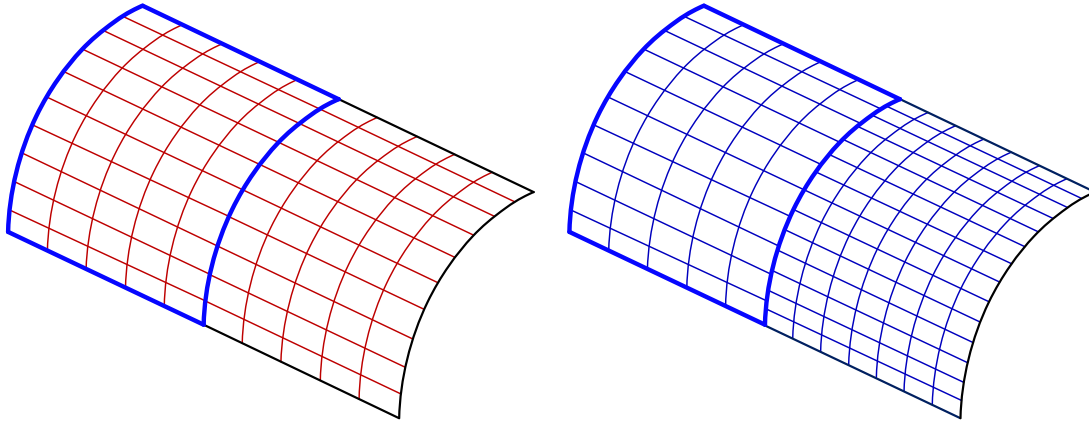
Figure 15: Meshes for the matching (left) and non-matching (right) cases of the nonlinear semi-cylinder problem. Black lines indicate patch boundaries and the thicker blue lines indicate continuum shell patches.

3.3. Nonlinear pinched semi-cylindrical shell

The proposed blended coupling approach is also applicable to multi-layered composite materials. In this example, a nonlinear pinched semi-cylinder problem characterizing both isotropic and composite materials is employed. As illustrated in Figure 14, the semi-cylinder is clamped at one end and subjected to a downward point force at the other, while symmetry boundary conditions are applied to the longitudinal edges. For the case of the isotropic material, the material properties of $E = 2.0685 \times 10^7$ and $v = 0.3$ are adopted. For the case of the composite orthotropic material, the material properties are $E_L = 2.0685 \times 10^7$, $E_T = 0.517125 \times 10^7$, $G_{LT} = 0.7956 \times 10^7$, and $v_{LT} = v_{TT} = 0.3$, where the subscript L refers to the longitudinal direction that is parallel to the $0°$ fibers, and the subscript T denotes the in-plane transverse direction that is perpendicular to the fibers. Both the isotropic and orthotropic models comprise three layers, with each layer having an
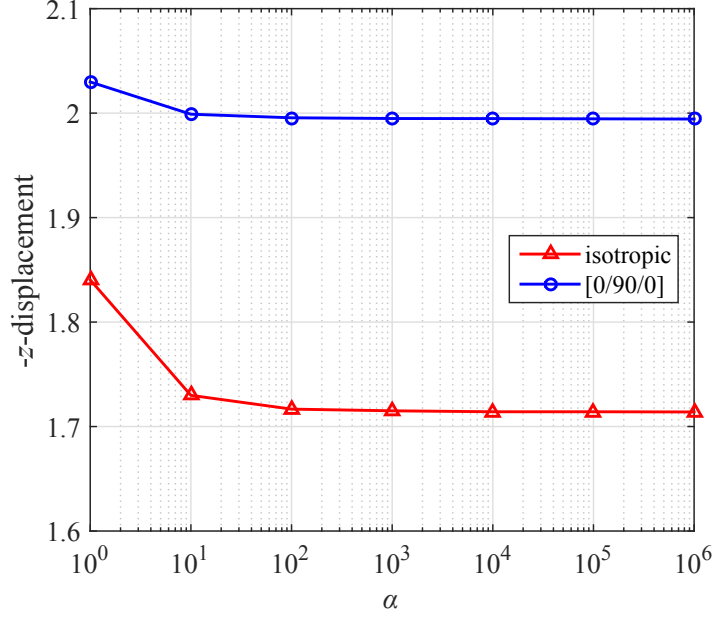
Figure 16: Ultimate vertical deflection at the point of applied force of the nonlinear semi-cylinder for varying α values. The analysis is performed using the matching discretization. The simulations with $\alpha = 10^7$ and beyond require very small load increments to converge due to the large penalty energy and are therefore abandoned.

equal thickness of 0.01 (i.e., the total thickness of the cylinder is $t_h = 0.03$). The ply orientation for the composite case is [0°/90°/0°]. A cylindrical arc-length algorithm [120] is adopted to solve this problem, where a loading factor λ ($0 < \lambda \leq 1$) is used to scale the total force of $F = 2000$.

Due to symmetry, only a half of the model is simulated. Two equally sized bicubic NURBS patches of matching and non-matching discretizations, as shown in Figure 15, are used to demonstrate the performance of the blended coupling approach in a nonlinear multi-layered analysis setting. The results shown below are obtained using one additional level of h-refinement from the discretizations in Figure 15.

The ultimate vertical deflection at the point of the applied force is plotted against a range of penalty coefficients, as shown in Figure 16. The analysis of this problem showed consistent solutions with the penalty coefficient α ranging from 10^2 to 10^6, which demonstrates the stability of the blended coupling approach and confirms the universal selection of a penalty value of $\alpha = 10^3$. Additionally, the load-displacement curve for the $\alpha = 10^3$ case is displayed in Figure 17 and compared with the reference data [119]. The solutions match very well with the reference results for both the matching and non-matching discretizations as well as both the isotropic and composite materials, demonstrating that the blended coupling approach is effective in a variety of applications.
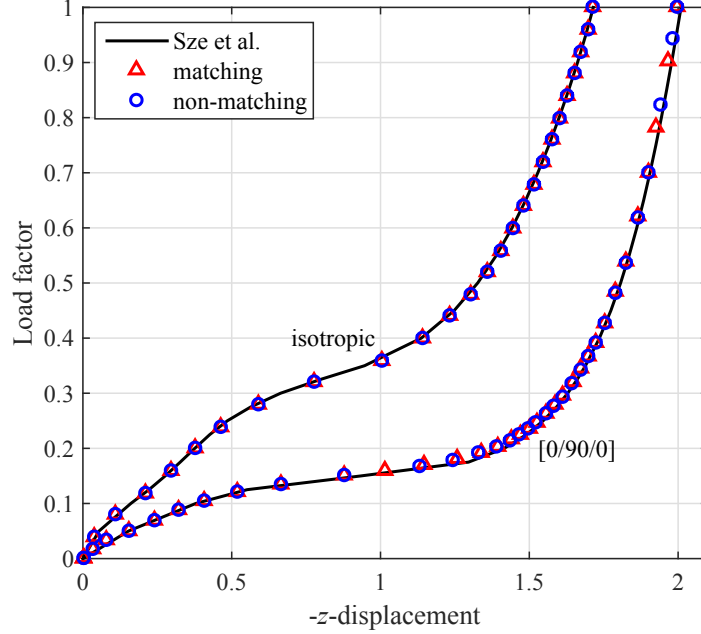
Figure 17: Load–displacement curve of the nonlinear semi-cylinder problem with $\alpha = 10^3$. The results are compared to the reference data from Sze et al. [119]. The load factor scales the maximum total force of $F = 2000$.

3.4. Composite square plate subjected to double sinusoidal load

The last example considered here is a geometrically linear benchmark problem that is intended to verify the accuracy of the complete 3D stress prediction using the proposed blended shell approach. Specifically, the classical composite square plate [84, 85, 121, 122], consisting of three layers of equal thickness, is tested under a double-sinusoidal pressure of magnitude q_0 at the top surface and is shown in Figure 18. The edges of the plate are simply supported, which is defined as $u_y = u_z = 0$ at the edges parallel to y and $u_x = u_z = 0$ at the edges parallel to x. The span-to-thickness ratio is $S = L/H = 4$, and the fiber orientations are $[0°/90°/0°]$. Orthotropic material properties are used with $E_1 = 2.5 \times 10^7$ psi, $E_2 = E_3 = 1.0 \times 10^6$ psi, $G_{12} = G_{13} = 0.5 \times 10^6$ psi, $G_{23} = 0.2 \times 10^6$ psi, and $\nu_{12} = \nu_{23} = \nu_{13} = 0.25$, where the subscript 1 denotes the direction parallel to the $0°$ fibers, the subscript 2 denotes the in-plane direction perpendicular to the $0°$ fibers, and the subscript 3 denotes the through-thickness direction. The double-sinusoidal pressure is specified as $q = q_0 \sin(\pi x/L) \sin(\pi y/L)$.

The plate is modeled with four equally sized bicubic NURBS patches, two with 4×4 elements and two with 5×5 elements, as shown in Figure 18. The non-matching discretization is coupled using the proposed penalty method with $\alpha = 10^3$. Only continuum shells are employed in this model in order to correctly apply the double-sinusoidal pressure at the top surface of the laminate and obtain the corresponding through-thickness stress states for comparison with the exact 3D elasticity solutions. Both cubic and quartic B-splines are utilized to describe the thickness displacement with
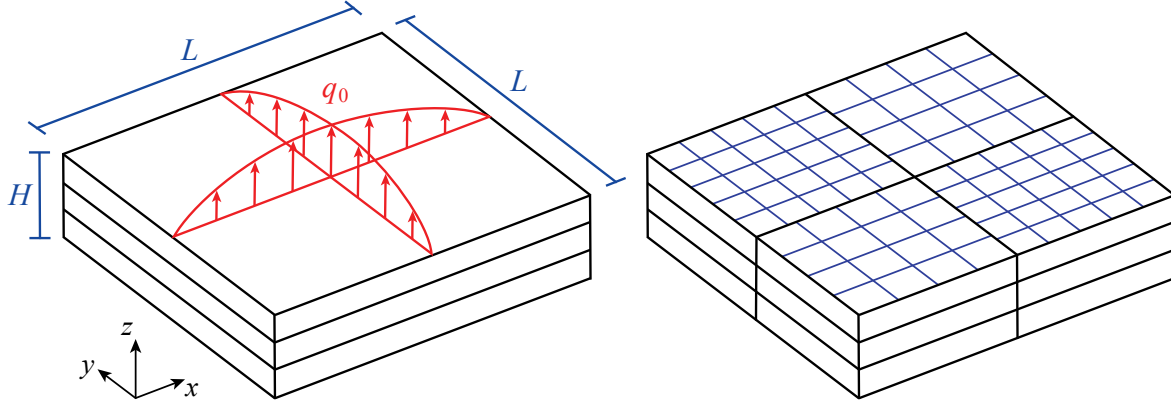
Figure 18: Problem setup and mesh discretization for a three-layer composite square plate subjected to double sinusoidal load.

only one thickness element per ply. The computed stress results are compared with the analytical solutions in Pagano [121], where the stress components are non-dimensionalized as follows [122]:

$$\bar{\sigma}_{11} = \frac{\sigma_{11}(p_1, p_1, z)}{q_0 S^2}, \quad \bar{\sigma}_{33} = \frac{\sigma_{33}(p_1, p_1, z)}{q_0}, \tag{32}$$

$$\bar{\sigma}_{13} = \frac{\sigma_{13}(p_2, p_1, z)}{q_0 S}, \quad \bar{\sigma}_{23} = \frac{\sigma_{23}(p_1, p_2, z)}{q_0 S}, \tag{33}$$

with $p_1 = 0.552831L$ and $p_2 = 0.947169L$ being the specified location coordinates for stress comparison.

As demonstrated in Figure 19, the obtained stress results using cubic B-splines in the thickness direction already match very well with the analytical solutions, with barely noticeable differences at the ply interfaces. By employing quartic B-splines in the thickness direction, the non-physical stress jumps at dissimilar material interfaces are eliminated, and the results illustrate excellent agreement with the reference solutions. This study demonstrates that the adopted continuum shell formulation is capable of accurately predicting the full 3D stress states.

4. Application to aircraft horizontal stabilizer analysis

The real-world engineering application of the proposed isogeometric blended shell approach is demonstrated through an example problem of nonlinear deflection analysis of an aircraft horizontal stabilizer. In aerospace engineering applications, horizontal stabilizers can be vulnerable to fatigue failure induced by flow separation from the aircraft wings and its impingement on the stabilizer structure in its wake. Consequently, the sustainment and repair of such structures necessitate the 3D stress information for multiaxial fatigue assessment. However, performing a high-fidelity nonlinear dynamic analysis of large-scale aircraft structures is time-consuming, and it is unrealistic to model
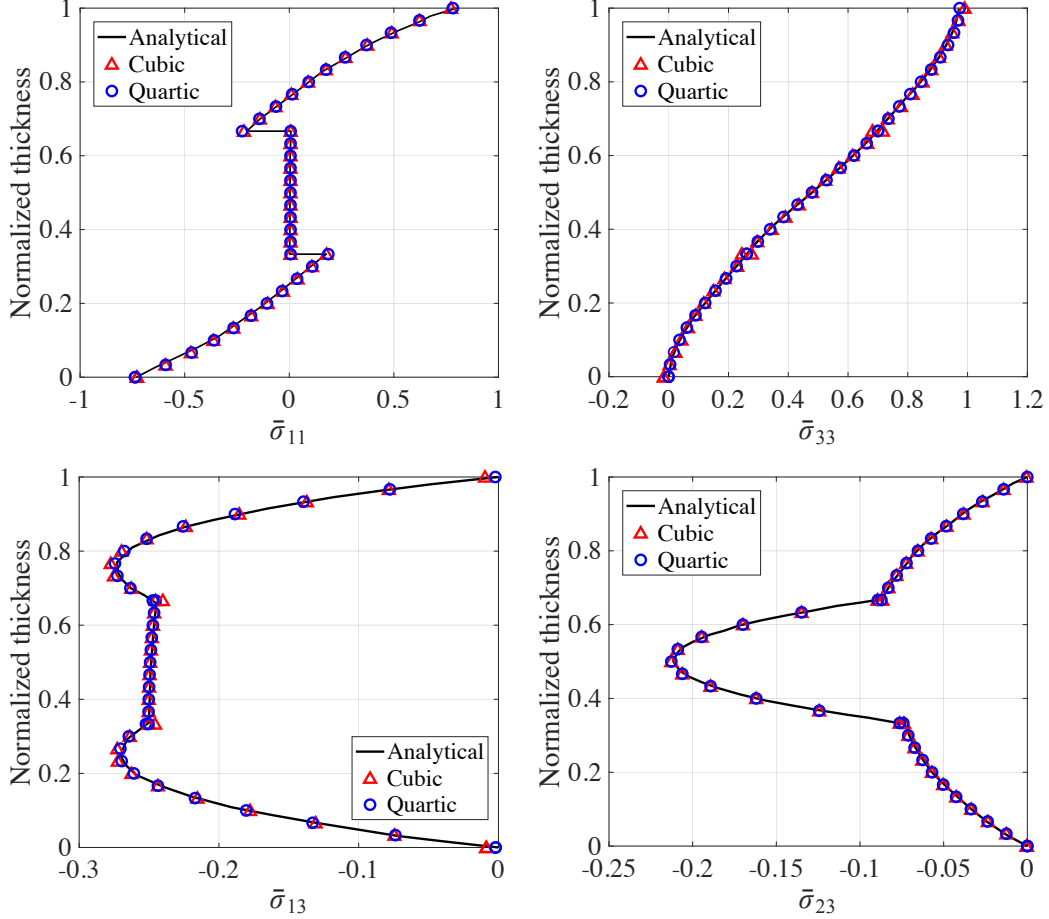
Figure 19: The normalized through-thickness stress distributions of the composite square plate.

the entire structure using continuum shells. In this context, the developed blended shell approach becomes an ideal candidate for the modeling of aircraft horizontal stabilizers, in which critical components can be modeled using continuum shells for high-fidelity stress prediction and other components can be modeled using KL shells to achieve computational efficiency.

A simplified horizontal stabilizer design, shown in Figure 20, is considered in this work. The design has a root chord length of 3.19 m, tip chord length of 0.7 m, and a tail semi-span of 6.75 m. The design consists of a skin and several internal rib and spar structures, which are modeled using 21 bicubic NURBS patches (six skin patches, ten rib patches, and five spar patches) that are coupled with a total of 71 penalty curves. Figure 21 shows the NURBS discretization of the stabilizer geometry with internal structures, where the patch enclosed by the thicker blue edges is modeled using continuum shells and all other remaining patches are modeled using KL shells. The thickness information of each section is given in Table 1. The material is assumed to be aluminum for all the sections with a Young's modulus of $E = 71.7$ GPa and Poisson's ratio of $\nu = 0.33$. A uniformly distributed traction load of 100 kPa in the $-z$ direction is applied on the skin patches, and the root

26
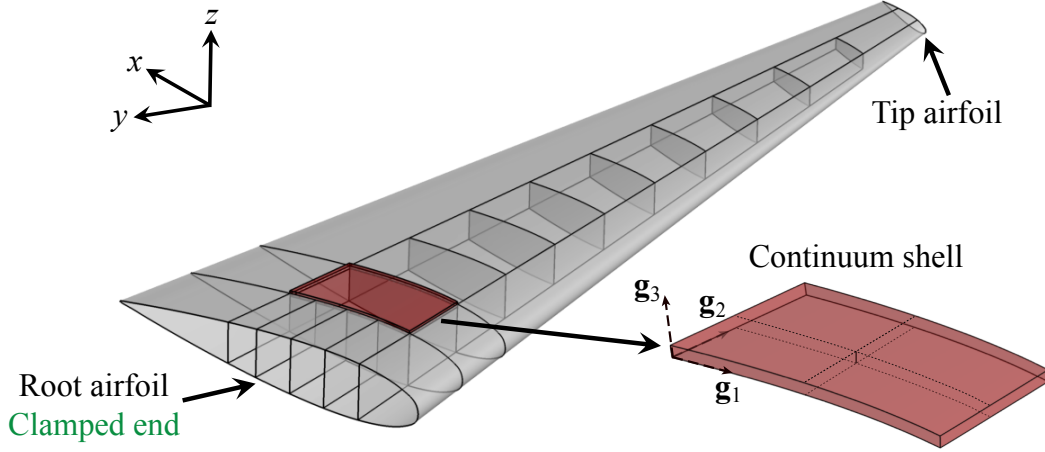
Figure 20: Aircraft horizontal stabilizer geometry showing skin, ribs, and spars. x, y and z indicate the global coordinate system. The highlighted region indicates the continuum shell patch. $\mathbf{g}_i$ are the base vectors of the covariant system for the continuum shell patch. The 3D stresses through the thickness will be extracted at the center of the continuum shell patch, as indicated by a through-thickness line.
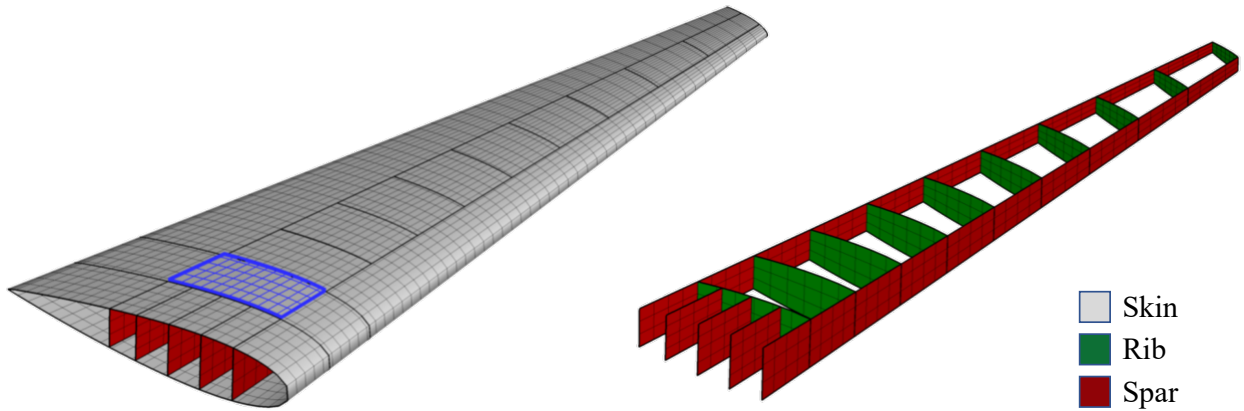
Figure 21: NURBS discretization of the horizontal stabilizer geometry. Thicker edges indicate the patch boundaries. Blue edges and mesh lines indicate patches modeled using continuum shells and the black edges and mesh lines indicate the patches modeled using KL shells.

end of the stabilizer skin is clamped. The nonlinear static deformation analysis is carried out using the blended shell approach with $\alpha = 10^3$. The tip deflection in z at the trailing edge of the stabilizer is reported for the mesh convergence study and comparison with reference solutions.

The mesh convergence analysis of the blended shell approach is carried out by performing uniform h-refinement of the in-plane directions on the stabilizer patches, as shown in Table 2. In order to obtain reference solutions, the nonlinear behavior of the same stabilizer is simulated using the commercial software Abaqus with S4 shell elements [123] and using pure isogeometric KL shells. In the case of pure isogeometric KL shells, the continuum shell patch in Figure 20 is replaced by a KL shell patch, and the simulation is performed using the proposed pure KL shell penalty coupling approach. The mesh statistics and the converged tip deflections obtained with

Table 1: Thickness information for different sections of the stabilizer.

Section	Number of patches	Thickness (m)
Skin	6	0.04
Ribs	10	0.01
Spars	5	0.01

Table 2: Mesh statistics and z-displacement of the trailing edge at the tip location computed using different meshes with the blended shell approach. Mesh 2 is shown in Figure 21.

Mesh	Number of elements	Number of DOFs	z-displacement (m)
1	954	6066	−0.279
2	3436	15951	−0.394
3	13744	52761	−0.399

Table 3: Solution comparison in terms of the maximum $-z$-displacement between the Abaqus reference solution, the pure KL shell penalty coupling approach, and the proposed blended shell approach. The IGA solutions are obtained using Mesh 3.

Method	Number of elements	Number of DOFs	Converged z-displacement (m)
Abaqus S4	44410	261720	−0.401
KL shell	13744	50331	−0.399
Blended shell	13744	52761	−0.399

various methods are reported in Table 3, where excellent agreement can be found between the Abaqus S4 model, the pure KL shell model, and the proposed blended shell model. The deformed configurations of the stabilizer from both the KL shell and the blended shell analyses are also shown in Figure 22, where the trailing-edge deflections at the tip are highlighted. The contour plots illustrate a smooth deformation field with excellent agreement of the tip deflections.

In order to showcase the capability of the blended shell approach in high-fidelity stress predictions, the through-thickness distributions of the 3D Cauchy stress tensor at the center of the continuum shell patch (as indicated in Figure 20) are extracted and shown in Figure 23. The stress components are defined with respect to the local Cartesian coordinate system, $\mathbf{e}_i$. Within this convention, $\mathbf{e}_1$ is aligned with $\mathbf{g}_1$ along the airfoil direction, $\mathbf{e}_3$ is aligned in the thickness direction, $\mathbf{g}_3$, which points from the inner to the outer surface of the stabilizer, and $\mathbf{e}_2 = \mathbf{e}_3 \times \mathbf{e}_1$ is the in-plane direction perpendicular to $\mathbf{g}_1$ that points from the root to the tip of the stabilizer (see Figure 20). The in-plane stress components σ_{11}, σ_{22}, and σ_{12} obtained using the pure KL shell approach are also plotted for comparison with the results from the blended shell analysis. As shown in Figure 23, the through-thickness distributions of the stress components from the pure KL shell analysis are

(a) KL shell　　　　　　　　　　　(b) Blended shell
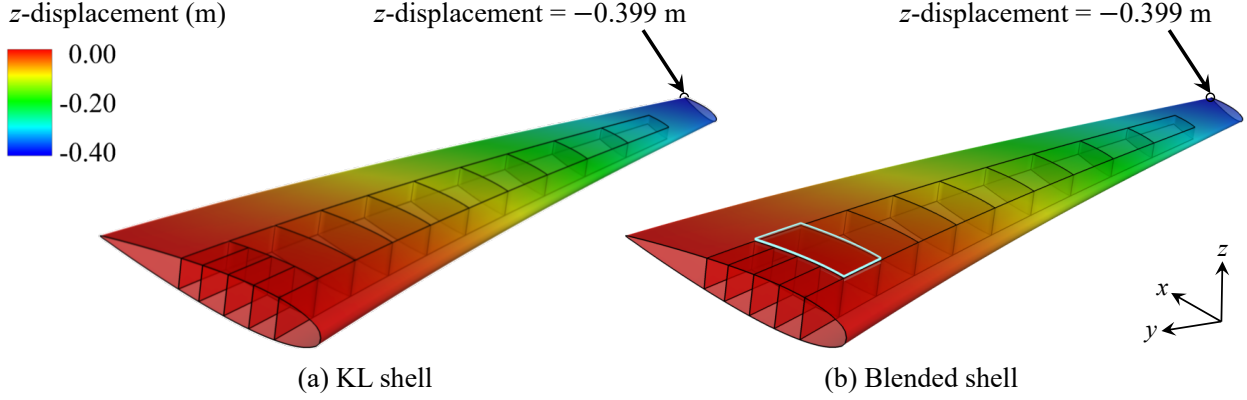
Figure 22: Displacement contour of the horizontal stabilizer for (a) KL shell and (b) blended shell analysis. The maximum $-z$-displacement recorded is indicated. The lighter blue lines indicate the boundary edges of the continuum patch.
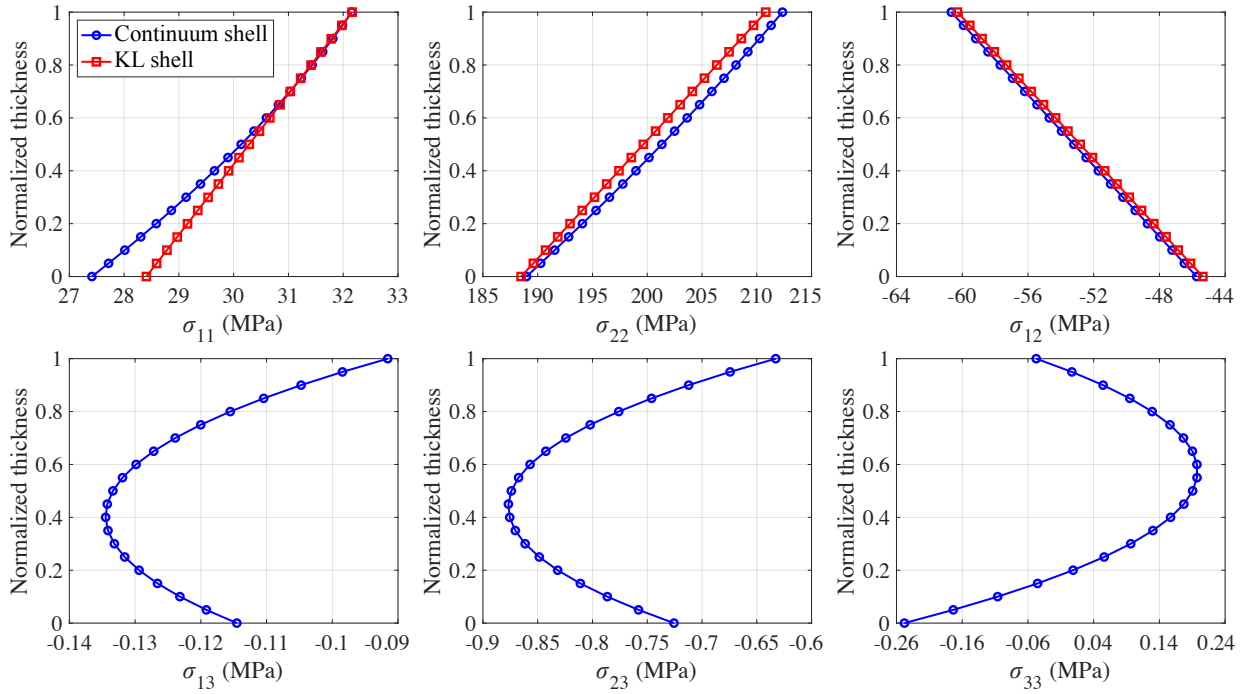
Figure 23: Through-thickness Cauchy stress distributions at the center of the continuum shell patch (see Figure 20). The stress at the center of the corresponding KL shell patch is also extracted for comparison. The stress components are defined with respect to the local Cartesian coordinate system. The subscript 1 denotes the direction along the airfoil that is aligned with $\mathbf{g}_1$, the subscript 2 denotes the in-plane direction perpendicular to $\mathbf{g}_1$ that points from the root to the tip, and the subscript 3 denotes the thickness direction that is aligned with $\mathbf{g}_3$, which points from the inner to the outer surface of the stabilizer.

linear, which is consistent with the KL shell assumption. By further comparing the in-plane stress components between the KL shell and the continuum shell, the magnitude and overall behavior of the stress components are relatively consistent; however, this comparison also reveals the lack of accuracy in predicting the nonlinear through-thickness stress states using KL shells. Additionally,

in contrast to the KL shell patches, where only the three in-plane stress components are directly available, the continuum shell patch captures the three additional stress components in the transverse direction. This information can be utilized for accurate multiaxial fatigue life evaluation and provides valuable guidance on the regular maintenance and repair of horizontal stabilizers.

5. Conclusion

An isogeometric blended shell approach that couples rotation-free KL and continuum shells is developed in this work. The key characteristic of the method is the inclusion of the penalty energies in the principle of virtual work to impose displacement and rotational continuities across interfaces of dissimilar shell types. The method primarily aims to provide compatibility between isogeometric KL and continuum shells and simulate large-scale structures in a high-fidelity and computationally efficient way by modeling critical structural components using continuum shells and other components using KL shells. The developed formulation adopts a dimensionally consistent penalty definition that yields accurate numerical performance across a wide range of applications. A dimensionless coefficient of $\alpha = 10^3$ is recommended as an appropriate, problem-independent penalty parameter that can be universally applied to different configurations. In addition, the method is applicable to non-matching and non-smooth interfaces joined at arbitrary angles as well as isotropic and composite materials.

The efficacy of the developed blended shell approach is demonstrated through a number of benchmark studies with a variety of problem configurations ranging from linear to nonlinear analyses, matching to non-matching discretizations, and isotropic to composite materials. In order to showcase the applicability of the blended shell approach to real-world engineering problems, an aircraft horizontal stabilizer with internal structures is modeled using 21 NURBS patches and 71 penalty coupling curves. The solutions obtained from the blended shell analysis showed excellent agreement with the solutions from the pure KL shell analysis and commercial software Abaqus. The through-thickness stress distributions at the center of the continuum shell patch are also extracted to highlight the utility of the blended shell approach for localized high-fidelity stress prediction. These results demonstrate the advantages of the developed blended shell methods for the analysis of large-scale engineering problems that require 3D stress information. Using the proposed approaches, these complex models can be simulated with manageable computational resources, and comprehensive stress distributions can be accurately predicted for the critical structural components.

References

[1] T. J. R. Hughes, J. A. Cottrell, and Y. Bazilevs. Isogeometric analysis: CAD, finite elements, NURBS, exact geometry and mesh refinement. *Computer Methods in Applied Mechanics and Engineering*, 194:4135–4195, 2005.

[2] L. Piegl and W. Tiller. *The NURBS Book (Monographs in Visual Communication), 2nd ed.* Springer-Verlag, New York, 1997.

[3] Y. Bazilevs, V. M. Calo, J. A. Cottrell, J. A. Evans, T. J. R. Hughes, S. Lipton, M. A. Scott, and T. W. Sederberg. Isogeometric analysis using T-splines. *Computer Methods in Applied Mechanics and Engineering*, 199:229–263, 2010.

[4] D. Schillinger, L. Dedè, M. A. Scott, J. A. Evans, M. J. Borden, E. Rank, and T. J. R. Hughes. An isogeometric design-through-analysis methodology based on adaptive hierarchical refinement of NURBS, immersed boundary methods, and T-spline CAD surfaces. *Computer Methods in Applied Mechanics and Engineering*, 249–252:116–150, 2012.

[5] W. Wang, Y. Zhang, L. Liu, and T. J. R. Hughes. Trivariate solid T-spline construction from boundary triangulations with arbitrary genus topology. *Computer-Aided Design*, 45:351–360, 2013.

[6] K. A. Johannessen, T. Kvamsdal, and T. Dokken. Isogeometric analysis using LR B-splines. *Computer Methods in Applied Mechanics and Engineering*, 269:471–514, 2014.

[7] N. Jaxon and X. Qian. Isogeometric analysis on triangulations. *Computer-Aided Design*, 46:45–57, 2014.

[8] A. Buffa and C. Giannelli. Adaptive isogeometric methods with hierarchical splines: error estimator and convergence. *Mathematical Models and Methods in Applied Sciences*, 26(01):1–25, 2016.

[9] X. Wei, Y. J. Zhang, and T. J. R. Hughes. Truncated hierarchical tricubic C^0 spline construction on unstructured hexahedral meshes for isogeometric analysis applications. *Computers & Mathematics with Applications*, 74:2203–2220, 2017.

[10] X. Wei, Y. Zhang, L. Liu, and T. J. R. Hughes. Truncated T-splines: Fundamentals and methods. *Computer Methods in Applied Mechanics and Engineering*, 316:349–372, 2017.

[11] S. Xia and X. Qian. Isogeometric analysis with Bézier tetrahedra. *Computer Methods in Applied Mechanics and Engineering*, 316:782–816, 2017.

[12] D. Toshniwal, H. Speleers, R. R. Hiemstra, and T. J. R. Hughes. Multi-degree smooth polar splines: A framework for geometric modeling and isogeometric analysis. *Computer Methods in Applied Mechanics and Engineering*, 316:1005–1061, 2017.

[13] X. Wei, Y. J. Zhang, D. Toshniwal, H. Speleers, X. Li, C. Manni, J. A. Evans, and

T. J. R. Hughes. Blended B-spline construction on unstructured quadrilateral and hexahedral meshes with optimal convergence rates in isogeometric analysis. *Computer Methods in Applied Mechanics and Engineering*, 341:609–639, 2018.

[14] Q. Zhang, M. Sabin, and F. Cirak. Subdivision surfaces with isogeometric analysis adapted refinement weights. *Computer-Aided Design*, 102:104–114, 2018.

[15] H. Casquero, X. Wei, D. Toshniwal, A. Li, T. J. R. Hughes, J. Kiendl, and Y. Zhang. Seamless integration of design and Kirchhoff–Love shell analysis using analysis-suitable unstructured T-splines. *Computer Methods in Applied Mechanics and Engineering*, 360:112765, 2020.

[16] R. R. Hiemstra, K. M. Shepherd, M. J. Johnson, L. Quan, and T. J. R. Hughes. Towards untrimmed NURBS: CAD embedded reparameterization of trimmed B-rep geometry using frame-field guided global parameterization. *Computer Methods in Applied Mechanics and Engineering*, 369:113227, 2020.

[17] G. Lorenzo, M. A. Scott, K. Tew, T. J. R. Hughes, Y. Zhang, L. Liu, G. Vilanova, and H. Gomez. Tissue-scale, personalized modeling and simulation of prostate cancer growth. *Proceedings of the National Academy of Sciences*, 113(48):E7663–E7671, 2016.

[18] K. Takizawa, T. E. Tezduyar, and T. Terahara. Ram-air parachute structural and fluid mechanics computations with the space–time isogeometric analysis (ST-IGA). *Computers & Fluids*, 141:191–200, 2016.

[19] Y. Lai, Y. J. Zhang, L. Liu, X. Wei, E. Fang, and J. Lua. Integrating CAD with Abaqus: A practical isogeometric analysis software platform for industrial applications. *Computers & Mathematics with Applications*, 74:1648–1660, 2017.

[20] Y. Otoguro, K. Takizawa, T. E. Tezduyar, K. Nagaoka, and S. Mei. Turbocharger turbine and exhaust manifold flow computation with the Space–Time Variational Multiscale Method and Isogeometric Analysis. *Computers & Fluids*, 179:764–776, 2019.

[21] T. Kanai, K. Takizawa, T. E. Tezduyar, T. Tanaka, and A. Hartmann. Compressible-flow geometric-porosity modeling and spacecraft parachute computation with isogeometric discretization. *Computational Mechanics*, 63:301–321, 2019.

[22] Y. Yu, Y. J. Zhang, K. Takizawa, T. E. Tezduyar, and T. Sasaki. Anatomically realistic lumen motion representation in patient-specific space–time isogeometric flow analysis of coronary arteries with time-dependent medical-image data. *Computational Mechanics*, 65:395–404, 2020.

[23] Y. Otoguro, K. Takizawa, T. E. Tezduyar, K. Nagaoka, R. Avsar, and Y. Zhang. Space–time VMS flow analysis of a turbocharger turbine with isogeometric discretization: Computa-

tions with time-dependent and steady-inflow representations of the intake/exhaust cycle. *Computational Mechanics*, 64:1403–1419, 2019.

[24] J. Yan, S. Lin, Y. Bazilevs, and G. J. Wagner. Isogeometric analysis of multi-phase flows with surface tension and with application to dynamics of rising bubbles. *Computers & Fluids*, 179:777–789, 2019.

[25] G. Lorenzo, T. J. R. Hughes, P. Dominguez-Frojan, A. Reali, and H. Gomez. Computer simulations suggest that prostate enlargement due to benign prostatic hyperplasia mechanically impedes prostate cancer growth. *Proceedings of the National Academy of Sciences*, 116:1152–1161, 2019.

[26] T. Terahara, K. Takizawa, T. E. Tezduyar, A. Tsushima, and K. Shiozaki. Ventricle-valve-aorta flow analysis with the Space–Time Isogeometric Discretization and Topology Change. *Computational Mechanics*, 65:1343–1363, 2020.

[27] T. Terahara, K. Takizawa, T. E. Tezduyar, Y. Bazilevs, and M.-C. Hsu. Heart valve isogeometric sequentially-coupled FSI analysis with the space–time topology change method. *Computational Mechanics*, 65:1167–1187, 2020.

[28] E. L. Johnson, M. C. H. Wu, F. Xu, N. M. Wiese, M. R. Rajanna, A. J. Herrema, B. Ganapathysubramanian, T. J. R. Hughes, M. S. Sacks, and M.-C. Hsu. Thinner biological tissues induce leaflet flutter in aortic heart valve replacements. *Proceedings of the National Academy of Sciences*, 117:19007–19016, 2020.

[29] D. J. Benson, Y. Bazilevs, E. De Luycker, M.-C. Hsu, M. Scott, T. J. R. Hughes, and T. Belytschko. A generalized finite element formulation for arbitrary basis functions: from isogeometric analysis to XFEM. *International Journal for Numerical Methods in Engineering*, 83:765–785, 2010.

[30] D. J. Benson, Y. Bazilevs, M.-C. Hsu, and T. J. R. Hughes. A large deformation, rotation-free, isogeometric shell. *Computer Methods in Applied Mechanics and Engineering*, 200: 1367–1378, 2011.

[31] D. J. Benson, S. Hartmann, Y. Bazilevs, M.-C. Hsu, and T. J. R. Hughes. Blended isogeometric shells. *Computer Methods in Applied Mechanics and Engineering*, 255:133–146, 2013.

[32] S. Morganti, F. Auricchio, D. J. Benson, F. I. Gambarin, S. Hartmann, T. J. R. Hughes, and A. Reali. Patient-specific isogeometric structural analysis of aortic valve closure. *Computer Methods in Applied Mechanics and Engineering*, 284:508–520, 2015.

[33] N. Liu and A. E. Jeffers. A geometrically exact isogeometric Kirchhoff plate: Feature-preserving automatic meshing and C^1 rational triangular Bézier spline discretizations. *In-*

ternational Journal for Numerical Methods in Engineering, 115(3):395–409, 2018.

[34] D. Kamensky, F. Xu, C.-H. Lee, J. Yan, Y. Bazilevs, and M.-C. Hsu. A contact formulation based on a volumetric potential: Application to isogeometric simulations of atrioventricular valves. *Computer Methods in Applied Mechanics and Engineering*, 330:522–546, 2018.

[35] K. Takizawa, T. E. Tezduyar, H. Uchikawa, T. Terahara, T. Sasaki, and A. Yoshida. Mesh refinement influence and cardiac-cycle flow periodicity in aorta flow analysis with isogeometric discretization. *Computers & Fluids*, 179:790–798, 2019.

[36] N. Liu and A. E. Jeffers. Feature-preserving rational Bézier triangles for isogeometric analysis of higher-order gradient damage models. *Computer Methods in Applied Mechanics and Engineering*, 357:112585, 2019.

[37] N. Liu, A. E. Jeffers, and P. A. Beata. A mixed isogeometric analysis and control volume approach for heat transfer analysis of nonuniformly heated plates. *Numerical Heat Transfer, Part B: Fundamentals*, 75(6):347–362, 2019.

[38] A. J. Herrema, J. Kiendl, and M.-C. Hsu. A framework for isogeometric-analysis-based optimization of wind turbine blade structures. *Wind Energy*, 22:153–170, 2019.

[39] J. Kiendl, K.-U. Bletzinger, J. Linhard, and R. Wüchner. Isogeometric shell analysis with Kirchhoff–Love elements. *Computer Methods in Applied Mechanics and Engineering*, 198: 3902–3914, 2009.

[40] J. Kiendl, M.-C. Hsu, M. C. H. Wu, and A. Reali. Isogeometric Kirchhoff–Love shell formulations for general hyperelastic materials. *Computer Methods in Applied Mechanics and Engineering*, 291:280–303, 2015.

[41] A. Buganza Tepole, H. Kabaria, K.-U. Bletzinger, and E. Kuhl. Isogeometric Kirchhoff–Love shell formulations for biological membranes. *Computer Methods in Applied Mechanics and Engineering*, 293:328–347, 2015.

[42] A. Riffnaller-Schiefer, U. H. Augsdörfer, and D. W. Fellner. Isogeometric shell analysis with NURBS compatible subdivision surfaces. *Applied Mathematics and Computation*, 272:139–147, 2016.

[43] H. Casquero, L. Liu, Y. Zhang, A. Reali, J. Kiendl, and H. Gomez. Arbitrary-degree T-splines for isogeometric analysis of fully nonlinear Kirchhoff–Love shells. *Computer-Aided Design*, 82:140–153, 2017.

[44] K. Takizawa, T. E. Tezduyar, and T. Sasaki. Isogeometric hyperelastic shell analysis with out-of-plane deformation mapping. *Computational Mechanics*, 63:681–700, 2019.

[45] M. Ambati, J. Kiendl, and L. De Lorenzis. Isogeometric Kirchhoff–Love shell formulation for elasto-plasticity. *Computer Methods in Applied Mechanics and Engineering*, 340:320–

339, 2018.

[46] M. Zareh and X. Qian. Kirchhoff–Love shell formulation based on triangular isogeometric analysis. *Computer Methods in Applied Mechanics and Engineering*, 347:853–873, 2019.

[47] G. D. Huynh, X. Zhuang, H. G. Bui, G. Meschke, and H. Nguyen-Xuan. Elasto-plastic large deformation analysis of multi-patch thin shells by isogeometric approach. *Finite Elements in Analysis and Design*, 173:103389, 2020.

[48] M. Breitenberger, A. Apostolatos, B. Philipp, R. Wüchner, and K.-U. Bletzinger. Analysis in computer aided design: Nonlinear isogeometric B-Rep analysis of shell structures. *Computer Methods in Applied Mechanics and Engineering*, 284:401–457, 2015.

[49] M.-C. Hsu, C. Wang, A. J. Herrema, D. Schillinger, A. Ghoshal, and Y. Bazilevs. An interactive geometry modeling and parametric design platform for isogeometric analysis. *Computers and Mathematics with Applications*, 70:1481–1500, 2015.

[50] J. Yan, B. Augier, A. Korobenko, J Czarnowski, G Ketterman, and Y. Bazilevs. FSI modeling of a propulsion system based on compliant hydrofoils in a tandem configuration. *Computers & Fluids*, 141:201–211, 2016.

[51] J. Kiendl, M. Ambati, L. De Lorenzis, H. Gomez, and A. Reali. Phase-field description of brittle fracture in plates and shells. *Computer Methods in Applied Mechanics and Engineering*, 312:374–394, 2016.

[52] M. C. H. Wu, D. Kamensky, C. Wang, A. J. Herrema, F. Xu, M. S. Pigazzini, A. Verma, A. L. Marsden, Y. Bazilevs, and M.-C. Hsu. Optimizing fluid–structure interaction systems with immersogeometric analysis and surrogate modeling: Application to a hydraulic arresting gear. *Computer Methods in Applied Mechanics and Engineering*, 316:668–693, 2017.

[53] L. Heltai, J. Kiendl, A. DeSimone, and A. Reali. A natural framework for isogeometric fluid–structure interaction based on BEM–shell coupling. *Computer Methods in Applied Mechanics and Engineering*, 316:522–546, 2017.

[54] Y. Guo, J. Heller, T. J. R. Hughes, M. Ruess, and D. Schillinger. Variationally consistent isogeometric analysis of trimmed thin shells at finite deformations, based on the STEP exchange format. *Computer Methods in Applied Mechanics and Engineering*, 336:39–79, 2018.

[55] T. Teschemacher, A. M. Bauer, T. Oberbichler, M. Breitenberger, R. Rossi, R. Wüchner, and K.-U. Bletzinger. Realization of CAD-integrated shell simulation based on isogeometric B-Rep analysis. *Advanced Modeling and Simulation in Engineering Sciences*, 5:19, 2018.

[56] M. S. Pigazzini, D. Kamensky, D. A. P. van Iersel, M. D. Alaydin, J. J. C. Remmers, and Y. Bazilevs. Gradient-enhanced damage modeling in Kirchhoff–Love shells: Application

to isogeometric analysis of composite laminates. *Computer Methods in Applied Mechanics and Engineering*, 346:152–179, 2019.

[57] L. F. Leidinger, M. Breitenberger, A. M. Bauer, S. Hartmann, R. Wüchner, K.-U. Bletzinger, F. Duddeck, and L. Song. Explicit dynamic isogeometric B-Rep analysis of penalty-coupled trimmed NURBS shells. *Computer Methods in Applied Mechanics and Engineering*, 351: 891–927, 2019.

[58] D. Kamensky and Y. Bazilevs. tIGAr: Automating isogeometric analysis with FEniCS. *Computer Methods in Applied Mechanics and Engineering*, 344:477–498, 2019.

[59] A. Nitti, J. Kiendl, A. Reali, and M. D. de Tullio. An immersed-boundary/isogeometric method for fluid–structure interaction involving thin shells. *Computer Methods in Applied Mechanics and Engineering*, 364:112977, 2020.

[60] K. Paul, C. Zimmermann, K. K. Mandadapu, T. J. R. Hughes, C. M. Landis, and R. A. Sauer. An adaptive space-time phase field formulation for dynamic fracture of brittle shells based on LR NURBS. *Computational Mechanics*, 65:1039–1062, 2020.

[61] D. Proserpio, M. Ambati, L. De Lorenzis, and J. Kiendl. A framework for efficient isogeometric computations of phase-field brittle fracture in multipatch shell structures. *Computer Methods in Applied Mechanics and Engineering*, 372:113363, 2020.

[62] Y. Bazilevs, M.-C. Hsu, J. Kiendl, R. Wüchner, and K.-U. Bletzinger. 3D simulation of wind turbine rotors at full scale. Part II: Fluid–structure interaction modeling with composite blades. *International Journal for Numerical Methods in Fluids*, 65:236–253, 2011.

[63] Y. Bazilevs, M.-C. Hsu, and M.A. Scott. Isogeometric fluid–structure interaction analysis with emphasis on non-matching discretizations, and with application to wind turbines. *Computer Methods in Applied Mechanics and Engineering*, 249–252:28–41, 2012.

[64] M.-C. Hsu and Y. Bazilevs. Fluid–structure interaction modeling of wind turbines: simulating the full machine. *Computational Mechanics*, 50:821–833, 2012.

[65] A. Korobenko, M.-C. Hsu, I. Akkerman, J. Tippmann, and Y. Bazilevs. Structural mechanics modeling and FSI simulation of wind turbines. *Mathematical Models and Methods in Applied Sciences*, 23(2):249–272, 2013.

[66] Y. Bazilevs, A. Korobenko, X. Deng, and J. Yan. Novel structural modeling and mesh moving techniques for advanced fluid–structure interaction simulation of wind turbines. *International Journal for Numerical Methods in Engineering*, 102(3-4):766–783, 2014.

[67] Y. Bazilevs, X. Deng, A. Korobenko, F. Lanza di Scalea, M. D. Todd, and S. G. Taylor. Isogeometric fatigue damage prediction in large-scale composite structures driven by dynamic sensor data. *Journal of Applied Mechanics*, 82:091008, 2015.

[68] J. Yan, A. Korobenko, X. Deng, and Y. Bazilevs. Computational free-surface fluid–structure interaction with application to floating offshore wind turbines. *Computers & Fluids*, 141: 155–174, 2016.

[69] A. J. Herrema, N. M. Wiese, C. N. Darling, B. Ganapathysubramanian, A. Krishnamurthy, and M.-C. Hsu. A framework for parametric design optimization using isogeometric analysis. *Computer Methods in Applied Mechanics and Engineering*, 316:944–965, 2017.

[70] A. Korobenko, J. Yan, S. M. I. Gohari, S. Sarkar, and Y. Bazilevs. FSI simulation of two back-to-back wind turbines in atmospheric boundary layer flow. *Computers & Fluids*, 158: 167–175, 2017.

[71] Y. Bazilevs, J. Yan, X. Deng, and A. Korobenko. Computer modeling of wind turbines: 2. Free-surface FSI and fatigue-damage. *Archives of Computational Methods in Engineering*, 26:1101–1115, 2018.

[72] E. L. Johnson and M.-C. Hsu. Isogeometric analysis of ice accretion on wind turbine blades. *Computational Mechanics*, 66:311–322, 2020.

[73] M.-C. Hsu, D. Kamensky, Y. Bazilevs, M. S. Sacks, and T. J. R. Hughes. Fluid–structure interaction analysis of bioprosthetic heart valves: significance of arterial wall deformation. *Computational Mechanics*, 54:1055–1071, 2014.

[74] D. Kamensky, M.-C. Hsu, D. Schillinger, J. A. Evans, A. Aggarwal, Y. Bazilevs, M. S. Sacks, and T. J. R. Hughes. An immersogeometric variational framework for fluid–structure interaction: Application to bioprosthetic heart valves. *Computer Methods in Applied Mechanics and Engineering*, 284:1005–1053, 2015.

[75] M.-C. Hsu, D. Kamensky, F. Xu, J. Kiendl, C. Wang, M. C. H. Wu, J. Mineroff, A. Reali, Y. Bazilevs, and M. S. Sacks. Dynamic and fluid–structure interaction simulations of bioprosthetic heart valves using parametric design with T-splines and Fung-type material models. *Computational Mechanics*, 55:1211–1225, 2015.

[76] F. Xu, S. Morganti, R. Zakerzadeh, D. Kamensky, F. Auricchio, A. Reali, T. J. R. Hughes, M. S. Sacks, and M.-C. Hsu. A framework for designing patient-specific bioprosthetic heart valves using immersogeometric fluid–structure interaction analysis. *International Journal for Numerical Methods in Biomedical Engineering*, 34:e2938, 2018.

[77] M. C. H. Wu, R. Zakerzadeh, D. Kamensky, J. Kiendl, M. S. Sacks, and M.-C. Hsu. An anisotropic constitutive model for immersogeometric fluid–structure interaction analysis of bioprosthetic heart valves. *Journal of Biomechanics*, 74:23–31, 2018.

[78] A. Balu, S. Nallagonda, F. Xu, A. Krishnamurthy, M.-C. Hsu, and S. Sarkar. A deep learning framework for design and analysis of surgical bioprosthetic heart valves. *Scientific Reports*,

9:18560, 2019.

[79] F. Xu, E. L. Johnson, C. Wang, A. Jafari, C.-H. Yang, M. S. Sacks, A. Krishnamurthy, and M.-C. Hsu. Computational investigation of left ventricular hemodynamics following bioprosthetic aortic and mitral valve replacement. *Mechanics Research Communications*, 112:103604, 2021.

[80] D. Kamensky. Open-source immersogeometric analysis of fluid–structure interaction using FEniCS and tIGAr. *Computers and Mathematics with Applications*, 81:634–648, 2021.

[81] E. L. Johnson, D. W. Laurence, F. Xu, C. E. Crisp, A. Mir, H. M. Burkhart, C.-H. Lee, and M.-C. Hsu. Parameterization, geometric modeling, and isogeometric analysis of tricuspid valves. *Computer Methods in Applied Mechanics and Engineering*, published online: 113960, 2021.

[82] S. Hosseini, J. J. C. Remmers, C. V. Verhoosel, and R. de Borst. An isogeometric continuum shell element for non-linear analysis. *Computer Methods in Applied Mechanics and Engineering*, 271:1–22, 2014.

[83] S. Hosseini, J. J. C. Remmers, C. V. Verhoosel, and R. de Borst. Propagation of delamination in composite materials with isogeometric continuum shell elements. *International Journal for Numerical Methods in Engineering*, 102:159–179, 2014.

[84] Y. Guo and M. Ruess. A layerwise isogeometric approach for NURBS-derived laminate composite shells. *Composite Structures*, 124:300–309, 2015.

[85] N. Liu and A. E. Jeffers. Isogeometric analysis of laminated composite and functionally graded sandwich plates based on a layerwise displacement theory. *Composite Structures*, 176:143–153, 2017.

[86] N. Liu. *Non-uniform rational B-splines and rational Bézier triangles for isogeometric analysis of structural applications*. PhD thesis, University of Michigan, 2018.

[87] L. Leonetti, F. S. Liguori, D. Magisano, and G. Garcea. An efficient isogeometric solid-shell formulation for geometrically nonlinear analysis of elastic shells. *Computer Methods in Applied Mechanics and Engineering*, 331:159–183, 2018.

[88] C. Adams, M. Fagerström, and J. J. C. Remmers. Efficient modelling of delamination growth using adaptive isogeometric continuum shell elements. *Computational Mechanics*, 65:99–117, 2020.

[89] N. Liu, X. Ren, and J. Lua. An isogeometric continuum shell element for modeling the nonlinear response of functionally graded material structures. *Composite Structures*, 237:111893, 2020.

[90] N. Liu, X. Cui, J. Xiao, J. Lua, and N. Phan. A simplified continuum damage mechanics

based modeling strategy for cumulative fatigue damage assessment of metallic bolted joints. *International Journal of Fatigue*, 131:105302, 2020.

[91] J. Lemaitre. A continuous damage mechanics model for ductile fracture. *Journal of Engineering Materials and Technology*, 107:83–89, 1985.

[92] N. Liu and A. E. Jeffers. Adaptive isogeometric analysis in structural frames using a layer-based discretization to model spread of plasticity. *Computers & Structures*, 196:1–11, 2018.

[93] J. Kiendl, Y. Bazilevs, M.-C. Hsu, R. Wüchner, and K.-U. Bletzinger. The bending strip method for isogeometric analysis of Kirchhoff–Love shell structures comprised of multiple patches. *Computer Methods in Applied Mechanics and Engineering*, 199:2403–2416, 2010.

[94] A. Goyal and B. Simeon. On penalty-free formulations for multipatch isogeometric Kirchhoff–Love shells. *Mathematics and Computers in Simulation*, 136:78–103, 2017.

[95] Z. Lei, F. Gillot, and L. Jezequel. A C^0/G^1 multiple patches connection method in isogeometric analysis. *Applied Mathematical Modelling*, 39(15):4405–4420, 2015.

[96] L. Coox, F. Greco, O. Atak, D. Vandepitte, and W. Desmet. A robust patch coupling method for NURBS-based isogeometric analysis of non-conforming multipatch surfaces. *Computer Methods in Applied Mechanics and Engineering*, 316:235–260, 2017.

[97] L. F. Leidinger, M. Breitenberger, A. M. Bauer, S. Hartmann, R. Wüchner, K.-U. Bletzinger, F. Duddeck, and L. Song. Explicit dynamic isogeometric B-rep analysis of penalty-coupled trimmed NURBS shells. *Computer Methods in Applied Mechanics and Engineering*, 351: 891–927, 2019.

[98] T. X. Duong, F. Roohbakhshan, and R. A. Sauer. A new rotation-free isogeometric thin shell formulation and a corresponding continuity constraint for patch boundaries. *Computer Methods in Applied Mechanics and Engineering*, 316:43–83, 2017.

[99] A. J. Herrema, E. L. Johnson, D. Proserpio, M. C. H. Wu, J. Kiendl, and M.-C. Hsu. Penalty coupling of non-matching isogeometric Kirchhoff–Love shell patches with application to composite wind turbine blades. *Computer Methods in Applied Mechanics and Engineering*, 346:810–840, 2019.

[100] M. C. H. Wu, H. M. Muchowski, E. L. Johnson, M. R. Rajanna, and M.-C. Hsu. Immersogeometric fluid–structure interaction modeling and simulation of transcatheter aortic valve replacement. *Computer Methods in Applied Mechanics and Engineering*, 357:112556, 2019.

[101] L. Leonetti, F. S. Liguori, D. Magisano, J. Kiendl, A. Reali, and G. Garcea. A robust penalty coupling of non-matching isogeometric Kirchhoff–Love shell patches in large deformations. *Computer Methods in Applied Mechanics and Engineering*, 371:113289, 2020.

[102] M. Ruess, D. Schillinger, A. I. Özcan, and E. Rank. Weak coupling for isogeometric analysis of non-matching and trimmed multi-patch geometries. *Computer Methods in Applied Mechanics and Engineering*, 269:46–731, 2014.

[103] Y. Guo and M. Ruess. Nitsche's method for a coupling of isogeometric thin shells and blended shell structures. *Computer Methods in Applied Mechanics and Engineering*, 284: 881–905, 2015.

[104] J. Benzaken, J. A. Evans, S. F. McCormick, and R. Tamstorf. Nitsche's method for linear Kirchhoff–Love shells: Formulation, error analysis, and verification. *Computer Methods in Applied Mechanics and Engineering*, 374:113544, 2021.

[105] N. Nguyen-Thanh, K. Zhou, X. Zhuang, P. Areias, H. Nguyen-Xuan, Y. Bazilevs, and T. Rabczuk. Isogeometric analysis of large-deformation thin shells using RHT-splines for multiple-patch coupling. *Computer Methods in Applied Mechanics and Engineering*, 316: 1157–1178, 2017.

[106] W. Dornisch, G. Vitucci, and S. Klinkel. The weak substitution method – an application of the mortar method for patch coupling in NURBS-based isogeometric analysis. *International Journal for Numerical Methods in Engineering*, 103(3):205–234, 2015.

[107] E. Brivadis, A. Buffa, B. Wohlmuth, and L. Wunderlich. Isogeometric mortar methods. *Computer Methods in Applied Mechanics and Engineering*, 284:292–319, 2015.

[108] M. Dittmann, S. Schuß, B. Wohlmuth, and C. Hesch. Crosspoint modification for multi-patch isogeometric analysis. *Computer Methods in Applied Mechanics and Engineering*, 360:112768, 2020.

[109] S. Schuß, M. Dittmann, B. Wohlmuth, S. Klinkel, and C. Hesch. Multi-patch isogeometric analysis for Kirchhoff–Love shell elements. *Computer Methods in Applied Mechanics and Engineering*, 349:91–116, 2019.

[110] H. Parisch. A continuum-based shell theory for non-linear applications. *International Journal for Numerical Methods in Engineering*, 38(11):1855–1883, 1995.

[111] S. Hosseini, J. J. C. Remmers, C. V. Verhoosel, and R. de Borst. An isogeometric solid-like shell element for nonlinear analysis. *International Journal for Numerical Methods in Engineering*, 95:238–256, 2013.

[112] R. Bouclier, T. Elguedj, and A. Combescure. An isogeometric locking-free nurbs-based solid-shell element for geometrically nonlinear analysis. *International Journal for Numerical Methods in Engineering*, 101(10):774–808, 2015.

[113] J. F. Caseiro, R. A. F. Valente, A. Reali, J. Kiendl, F. Auricchio, and R. J. Alves de Sousa. Assumed natural strain nurbs-based solid-shell element for the analysis of large deformation

elasto-plastic thin-shell structures. *Computer Methods in Applied Mechanics and Engineering*, 284:861–880, 2015.

[114] J. F. Caseiro, R. A. Fontes Valente, A. Reali, J. Kiendl, F. Auricchio, and R. J. Alves De Sousa. On the assumed natural strain method to alleviate locking in solid-shell nurbs-based finite elements. *Computational Mechanics*, 53(6):1341–1353, 2014.

[115] P. Antolin, J. Kiendl, M. Pingaro, and A. Reali. A simple and effective method based on strain projections to alleviate locking in isogeometric solid shells. *Computational Mechanics*, pages 1–11, 2020.

[116] J. Kiendl. *Isogeometric Analysis and Shape Optimal Design of Shell Structures*. PhD thesis, Lehrstuhl für Statik, Technische Universität München, 2011.

[117] K. Takizawa, Y. Ueda, and T. E. Tezduyar. A node-numbering-invariant directional length scale for simplex elements. *Mathematical Models and Methods in Applied Sciences*, 29: 2719–2753, 2019.

[118] Y. Ueda, Y. Otoguro, K. Takizawa, and T. E. Tezduyar. Element-splitting-invariant local-length-scale calculation in B-Spline meshes for complex geometries. *Mathematical Models and Methods in Applied Sciences*, 30:2139–2174, 2020.

[119] K. Y. Sze, X. H. Liu, and S. H. Lo. Popular benchmark problems for geometric nonlinear analysis of shells. *Finite Elements in Analysis and Design*, 40:1551–1569, 2004.

[120] N. Liu, P. Plucinsky, and A. E. Jeffers. Combining load-controlled and displacement-controlled algorithms to model thermal-mechanical snap-through instabilities in structures. *Journal of Engineering Mechanics*, 143(8):04017051, 2017.

[121] N. J. Pagano. Exact solutions for rectangular bidirectional composites and sandwich plates. *Journal of Composite Materials*, 4:20–34, 1970.

[122] D. H. Robbins and J. N. Reddy. Modelling of thick composites using a layerwise laminate theory. *International Journal for Numerical Methods in Engineering*, 36(4):655–677, 1993.

[123] Abaqus Unified FEA. https://www.3ds.com/products-services/simulia/products/abaqus/. Accessed June 1, 2021.